Annals of Nuclear Energy 206 (2024) 110612

Contents lists available at ScienceDirect

Annals of Nuclear Energy

journal homepage: www.elsevier.com/locate/anucene

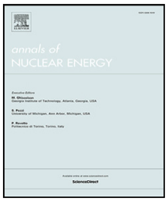

# Verification and validation of seven turbulence models for a natural circulation loop under transient conditions

G. Angelo [a,b,*], E. Angelo [a], N.L. Scuro [b,c], W.M. Torres [b], D.A. Andrade [b]

[a] School of Engineering, Mackenzie Presbyterian University, São Paulo, SP, Brazil
[b] Nuclear Engineering Center, Nuclear and Energy Research Institute, São Paulo, SP, Brazil
[c] Department of Energy and Nuclear Engineering, Ontario Tech University, Oshawa, ON, Canada

## ARTICLE INFO

*Keywords:*
Natural circulation loop
Turbulence model benchmarking
Natural convection
Spatial discretization
Temporal discretization
$k-\varepsilon$ model
Numerical simulation
Transient flow analysis
Verification and validation

## ABSTRACT

A numerical study of the vertical heater, vertical cooler (VHVC) natural circulation loop (NCL) at IPEN/CNEN-SP was conducted using a three-dimensional and transient mathematical model analyzed with the commercial software ANSYS CFX. The study focused on the stable and single-phase flow regime, with a Rayleigh number ranging from zero to $2.8\times10^8$. Seven turbulence models have been benchmarked: Zero Equation, Eddy Viscosity Transport Equation (EVTE), $k-\omega$, $k-\varepsilon$, Shear Stress Transport (SST), Reynolds Stress (SSG), and Detached Eddy Simulation (DES). The results of these models were compared against each other and against experimental results obtained specifically for this purpose, focusing on the spatial distribution and temporal evolution of temperature at various points in the natural circulation loop. Among all tested models, the $k-\varepsilon$ model demonstrated superior performance with the lowest average deviation, exhibiting lower initial turbulence production and buoyancy effects than the more complex models. This behavior suggests that the $k-\varepsilon$ model is more accurate in predicting temperature distribution and is a better choice for transient flow analysis in natural circulation loops with similar geometries to those presented in this study.

## 1. Introduction

The primary advantage of natural convection is the independence of fluid motion from mechanical devices like pumps or ventilators. This feature is critical in nuclear passive safety systems (Carelli et al., 2004) and has become a requirement for residual heat removal in fourth-generation nuclear reactors (Kelly, 2014; Talaat and Chen, 2023). Besides, natural convection plays a pivotal role in other practical applications, such as water heating systems, temperature control in electronic systems, or any scenario involving natural convection. The mechanism involves setting up natural circulation circuits and closed systems containing hot and cold sources linked by ducts. Arranging the hot source below the cold source creates a thermal gradient that propels fluid flow through the system. However, the design of these processes must account for how initial conditions affect the established flow pattern.

The growing trend towards numerical-computational simulations in the design of such systems makes it essential to understand when and why computational fluid dynamics (CFD) models are accurate. The increasing accessibility of computational tools, including commercial codes, has enabled engineers to use them for project analysis and development. These tools offer various modeling options, like the choice of turbulence models, which can yield different results depending on the flow conditions and the simulated geometry (Piña-Ortiz et al., 2014). However, these alternatives may lead to incorrect choices for the problem under investigation.

Many studies (Ji et al., 2023) have investigated natural convection in cavities or geometries where the hot and cold sources occupy nearly the same region. Other researchers have utilized vertical parallel walls with varying temperatures (Spiga and Vocale, 2015). The flow dynamics established in these cases can differ significantly from those occurring in natural circulation loops (NCL's). One reason is that the flow in natural circulation loops is confined by the duct walls connecting the hot and cold sources, thereby accentuating the effects of fluid viscosity on the flow due to the no-slip wall condition.

Early studies by Zvirin (1982) and Greif (1988) laid the foundation for exploring single-phase flow in natural circulation loops through experimental and theoretical analyses. A significant challenge in this area is the occurrence of instabilities, defined as deviations from a steady-state flow condition that leads to oscillatory or unsteady fluid behavior. These instabilities can be triggered by changes in the system's geometrical configuration, fluid properties, or heat transfer conditions (Vijayan, 2002).

---

[*] Corresponding author at: School of Engineering, Mackenzie Presbyterian University, São Paulo, SP, Brazil.
*E-mail address:* gabriel.angelo@mackenzie.br (G. Angelo).

https://doi.org/10.1016/j.anucene.2024.110612
Received 29 January 2024; Received in revised form 4 April 2024; Accepted 6 May 2024

Numerical studies, such as Angelo et al. (2012), have focused exclusively on steady-state conditions, employing a single turbulence model (Standard $k-\varepsilon$). These studies have achieved accuracy within acceptable engineering deviations by comparing numerical model responses with experimental results. Despite the noted limitations, such studies have provided valuable insights, revealing structures like vortices and recirculation effects, especially at the outlet of the natural circulation circuit heater.

Despite significant progress in the field, there is a need for studies under similar conditions to those conducted by Kim et al. (2021), who investigated various turbulence models in the internal flow of a rectangular duct. Other works have used simplifying assumptions, such as a uniform velocity in all regions of a particular duct cross-section (Zvirin, 1982; Greif, 1988; Huang and Zelaya, 1988; Jiang et al., 2002). While these methods help understand the overall flow, they cannot capture patterns containing vortices and recirculation.

Pilkhwal et al. (2007) conducted an in-depth analysis of the hydrodynamic stability of natural circulation circuits under single-phase flow conditions, revealing that one-dimensional models often fall short in accurately representing the dynamics of these systems. This inadequacy stems from various factors including, but not limited to, the disregard for boundary layer development, incorrect assumptions related to one-dimensional flow in proximity to heat exchangers, and inaccuracies arising from the underestimation of radial heat exchange between the ducts and the ambient environment.

Research conducted by Kudariyawar et al. (2016a,b) implemented computational fluid dynamics (CFD) to analyze the steady-state and transient characteristics of natural circulation loops utilizing two different working fluids: molten salt (a) and water (b). The molten salt study focused on a laminar flow regime, whereas the water-based investigation observed multiple flow behaviors. Their detailed analysis extended from exploring steady-state attributes to probing various transient phenomena and their impact on system stability. Even with the methodological parallels, our research, centered on a fluid that characterizes a turbulent flow regime, invites complexity when attempting a direct comparison due to the differing fluid properties and flow behaviors.

Significant advancements in this field have emphasized the impact of nanoparticle shape on thermal-hydraulic behavior in nanofluid-enhanced single-phase natural circulation loops. Investigations conducted by Sahu et al. (2023) using mono and hybrid nanofluids illuminated the substantial effect of nanoparticle shape on parameters such as mass flow rate, heat exchanger effectiveness, and total entropy generation rate under varying conditions.

Numerous rigorous studies have been conducted in the field of natural circulation loop simulations and experiments. Among them, we can cite Ryu et al. (2018) that concentrated on the natural circulation characteristics of a liquid metal coolant in advanced small modular reactors. Meanwhile, Cheng et al. (2018) carried out three-dimensional transient numerical simulations to delve into the heat transfer dynamics in single-phase natural circulation loops using water. In a different approach, Elton et al. (2022) focused on the stability behavior of series-coupled rectangular loops, uncovering a hysteresis phenomenon of instability thresholds and the role of wall structures in oscillation damping. On the other hand, Adinarayana et al. (2022) developed a numerical model to shed light on the transient performance of series-coupled natural circulation loops, pinpointing critical operational parameters. These substantial contributions to our understanding of efficient passive heat removal system design and operation are noteworthy.

Furthermore, Sarkar and Basu (2017) evaluated the thermal-hydraulic behaviors of water, $CO_2$, and R134a in a temperature-coupled natural circulation loop through computational investigation. The study underscored the benefits of supercritical conditions, mainly using supercritical $CO_2$ due to its exceptional performance under high pressure and low sink temperature conditions.

**Table 1**
Numerical and three-dimensional studies for natural circulation loops.

| Ref. | Exp. | Turb. Model |
|---|---|---|
| Piña-Ortiz et al. (2014) | x | Standard $k-\varepsilon$<br>Realizable $k-\varepsilon$<br>RNG $k-\varepsilon$<br>Reynolds Stress Model<br>Standard $k-w$<br>Shear-Stress $k-w$ |
| Ji et al. (2023) | – | Shear-Stress $k-w$<br>Large Eddy Simulation |
| Kelm et al. (2016) | x | Shear-Stress $k-w$ |
| Angelo et al. (2012) | x | Standard $k-\varepsilon$ |
| Cheng et al. (2018) | – | Laminar |
| Devia and Misale (2012) | x | not declared |
| Krishnani and Basu (2016) | – | RNG $k-\varepsilon$ |
| Kudariyawar et al. (2016a) | x | Laminar |
| Kudariyawar et al. (2016b) | – | Standard $k-\varepsilon$<br>Low-Reynolds number $k-\varepsilon$ |
| Pilkhwal et al. (2007) | – | RNG $k-\varepsilon$ |

Notes: Exp. = Comparison with experimental data.

Devia and Misale (2012) and Basu et al. (2012) made notable contributions to the study of single-phase natural circulation loops. Devia and Misale (2012) investigated instantaneous mass and heat flow rates in primary loop sections using CFD simulations, thereby enhancing our understanding of these systems. In parallel, Basu et al. (2012) developed a unified model applicable to different geometrical configurations. This model was validated against experimental results and was used to compare the performance of various loop shapes.

Table 1 summarizes the reference, indicating whether the study presents numerical or numerical experimental results, along with the turbulence models used. Despite the publication of numerous rigorous studies utilizing numerical-computational simulations on NCL's, there remains an open discussion in the literature regarding the effectiveness of different turbulence models. This is particularly evident even under conditions of stable, single-phase flow with simple geometry and arrangements, such as in VHVC (vertical heater, vertical cooler) systems.

In response to this gap, this article does not seek to present the unequivocal choice of a turbulence model. Instead, it aims to identify a potentially effective model for NCL analysis from a selection of seven turbulence models. The goal is to contribute to the ongoing discussion in the field, enhancing the understanding of how these models perform under specific conditions.

Table 1 includes the study by Piña-Ortiz et al. (2014), considered a reference for turbulence model studies. However, it is essential to note that the proposed geometry in this study is not precisely a natural circulation circuit but an inclined open cubic cavity. This configuration could lead to significantly different outcomes for natural circulation circuits.

This study focuses on the numerical analysis of a vertical heater, vertical cooler (VHVC) natural circulation loop at the Instituto de Pesquisas Energéticas e Nucleares – IPEN/CNEN-SP. We employ the commercial computational code ANSYS CFX to simulate single-phase, transient three-dimensional water flow in stable conditions, with a Rayleigh number ranging from zero to $2.8\times10^8$. The research tests various turbulence models, and the results are compared directly to experimental measurements for model validation. This work aims to identify the most suitable turbulence model among those tested, considering the defined experimental parameters and boundary conditions.

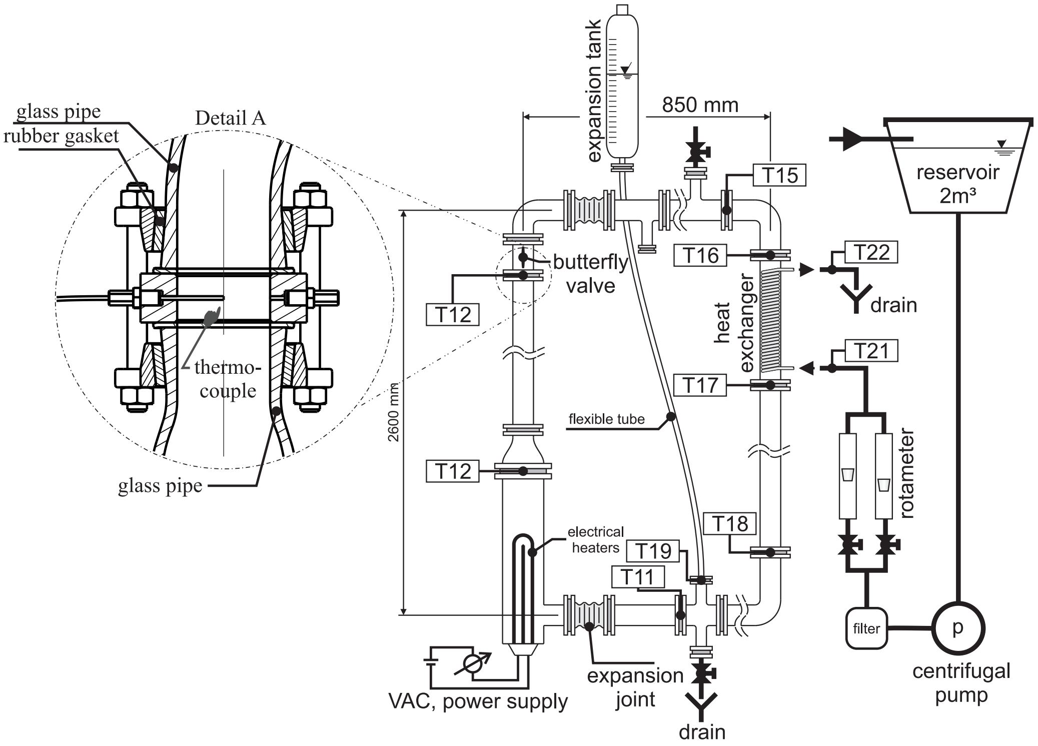

**Fig. 1.** Schematic drawing indicating the main rectangular loop dimensions, thermocouple positions, and principal devices.

## 2. Experimental apparatus

The experimental setup used in this study is a natural circulation loop with a rectangular geometry and a variable circular flow cross-section, as illustrated in Fig. 1. The loop consists of several components: two U-shaped electrical heaters (Fig. 2a), a single-pass counterflow heat exchanger with a shell and helical tubes (Fig. 2b), a cooling fluid reservoir, an expansion tank, expansion joints, a centrifugal pump, and a butterfly valve. The loop is entirely made of glass, which allows for flow visualization under two-phase flow conditions, and the fluid used in the loop and heat exchanger is water.

The loop has a total of twelve K-type thermocouples, with three positioned on the inner surface of the glass tube (TW1, TW2, and TW3), two thermocouples located at the inlet and outlet of the cooling fluid at the heat exchanger (T21 and T22), and the remaining thermocouples (T11 to T13, and T15 to T20) inserted in the centerline of the flow through flange joints, as indicated in Fig. 1 - detail A. These thermocouple positions were identified in Angelo et al. (2012) as fully developed flow points under steady-state conditions. A pressure transducer is also located above the electric heater, and two rotameters are used to adjust the mass flow rate of the heat exchanger.

The heating section consists of two electrical resistances, and the applied power can be controlled from 0 to 8400 W, with each electrical resistance ranging from 0 to 4200 W. The heat power is regulated through an alternating voltage controller.

Eight experimental tests were conducted to validate the mathematical model and verify the experiments' reproducibility with the same applied power to the heater. The nominal power applied to Heater 1 equals 1000 W, with only Electrical Heater 1 in operation. This power setting was chosen to ensure a stable and single-phase flow regime within the natural circulation loop. The mass flow rate was adjusted to 0.02772 ± 0.00138 kg/s in the helical tubes of the heat exchanger.

The authors acknowledge the limitation of the study in working exclusively with a nominal power configuration of 1000 W, identifying this constraint as significant in the analysis of the NCL. This specific power was chosen to ensure stable conditions, avoiding bubble nucleation on the surface of the electric resistance. However, it must be emphasized that the Rayleigh number of the loop varied from zero to $2.8 \times 10^8$, indicating that a significant spectrum of the flow behavior was captured within the established constraints. The Rayleigh number was obtained according to Eq. (1).

$$Ra = \frac{\beta \cdot g \cdot \Delta T \cdot L^3}{\nu^2} \cdot Pr \tag{1}$$

Where, $\Delta T$ is the temperature difference between the hot and cold leg of the loop under steady-state conditions, and $L$ is the hydraulic diameter of the cross-section in the heater region. The thermodynamic properties for the Rayleigh number were obtained using the mean temperature between the hot and cold leg.

The data acquisition system used in this study is a National Instruments Corporation setup consisting of two signal conditioner modules, two terminal blocks, and an acquisition PCMCIA card installed in a laptop computer. LabVIEW software is used to create a visual software interface.

The natural circulation loop is located at the Instituto de Pesquisas Energéticas e Nucleares (IPEN) - Comissão Nacional de Energia Nuclear (CNEN-SP) in São Paulo, Brazil. It is important to emphasize that this circuit, with different measurement conditions, has been utilized in various other studies, including Bueno et al. (2018), de Mesquita et al. (2018), Angelo et al. (2012), de Mesquita et al. (2012), Sabundjian et al. (2011), and Conti et al. (2011).

The temperature distribution of thermocouples T12 (hot leg) and T18 (cold leg) over time is presented in Figs. 3a and 3b, respectively, where the labels I to VIII represent experiments conducted on different days under the same operating conditions. While some dispersion in the data at the same instant is observed, the amplitude remains relatively consistent. This variability can be attributed to the significant challenge of ensuring the initial state of the circuit (due to factors such as thermal stratification) and maintaining a constant external environment temperature during the experiment.

In this natural circulation loop, there is an issue related to the onset of the transient process. The problem is associated with thermal stratification. Even after waiting for a relatively considerable time between experiments, temperature variations between the upper and

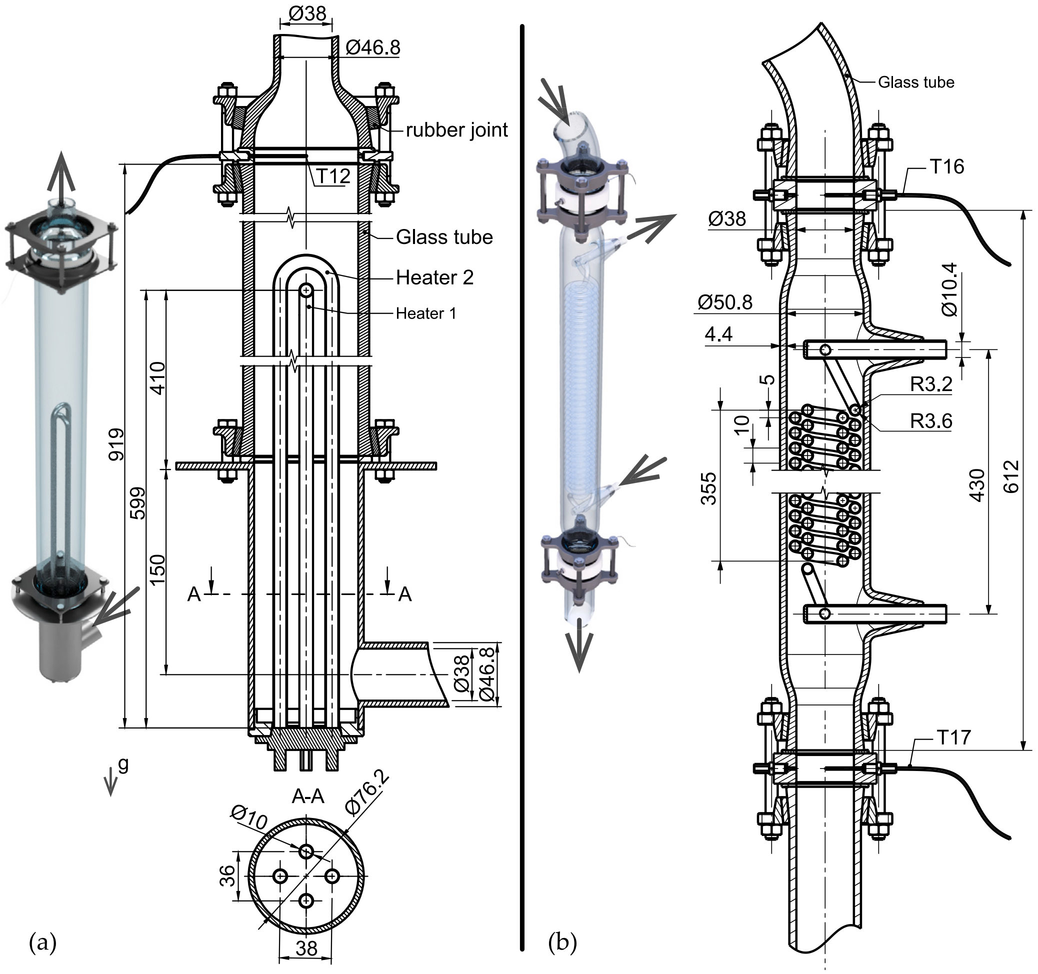

**Fig. 2.** Detail view of the main elements of the NCL, with dimensions in millimeters: (a) U-shaped electrical heaters; and (b) counterflow heat exchanger with shell and helical tubes.

lower parts of the device are always present in the circuit. Based on the experimental data, it is possible to identify an average variation of approximately 3.1 °C between the top and bottom of the circuit.

The average temperature ($\overline{T}(t)$) was calculated for the same instant using Eq. (2). Additionally, the standard deviation ($\sigma_m(t)$), reflecting the level of dispersion in the temperature data, was calculated using Eq. (3). At the beginning of the experiment, an increase in the standard deviation is observed. It can be attributed to slight delays in the start times of different experiments, resulting in variations in the rates of temperature change. The total uncertainty ($\sigma_T(t)$) associated with these measurements was calculated using Eq. (4). In this equation, $\sigma_r$ represents the uncertainty of the K-type thermocouples, determined to be ± 0.5 °C. Difficulties in establishing a homogeneous and identical initial temperature condition for the circuit, influenced by factors such as ambient temperature and persistent thermal stratification, contribute to the uncertainties observed at the start of the experiment.

$$\overline{T}(t) = \frac{1}{n}\sum_{i=1}^{n} T_i(t) \tag{2}$$

$$\sigma_m(t) = \sqrt{\frac{1}{n-1}\sum_{i=1}^{n}\left(T_i(t) - \bar{T}(t)\right)^2} \tag{3}$$

$$\sigma_T(t) = \sqrt{\sigma_m(t)^2 + \sigma_r(t)^2} \tag{4}$$

Fig. 4 shows the average temperature and total uncertainty for thermocouples T12 and T18 as a function of time. The other thermocouple data are presented alongside the numerical results of the turbulence

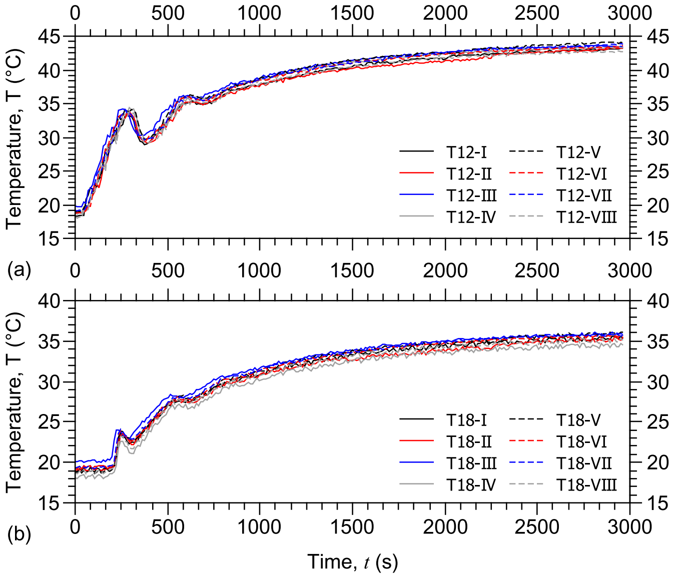

**Fig. 3.** Experiments I to VIII conducted on different days under the same conditions: (a) Temperature measurements for T12 – hot leg; (b) Temperature measurements for T18 – cold leg.

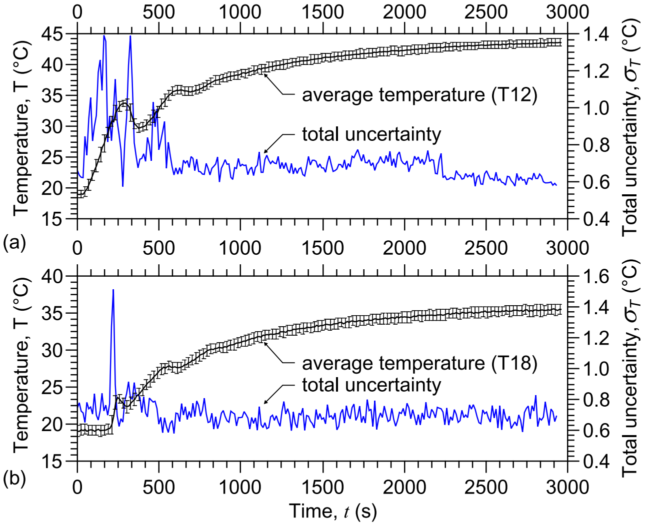

**Fig. 4.** (a) Average temperature for T12 thermocouple, indicating its total uncertainty as a function of time, and (b) average temperature for T18 thermocouple, indicating its total uncertainty as a function of time.

models. Notably, the maximum uncertainty for any measurement does not exceed 1.8 °C for all thermocouples used in the experiments.

The T19 and T20 thermocouples can be omitted in the absence of a two-phase flow regime. Despite the transient nature of the experiment, several quantities remain almost constant, including: (i) the power applied to Heater 1 at 1025.4 ± 19.9 W, (ii) the ambient temperature at 21.05 ± 1.05 °C, and (iii) the inlet temperature of the helical heat exchanger at 21.05 ± 1.06 °C.

## 3. Methodology

A three-dimensional transient mathematical model for the natural circulation loop was developed based on the finite volume method applied to a tetrahedral unstructured mesh (Darwish and Moukalled, 2016). The mass, momentum, and energy conservation equations are considered.

The buoyancy effect is modeled by the inclusion of a source term in the momentum equation, as shown in Eq. (5).

$$S_M = g_i \cdot (\rho - \rho_{ref}) \tag{5}$$

Since the pressure gradient is relatively small in the natural circulation loop and density variations are due only to temperature variations (Incropera and DeWitt, 1985), the Boussinesq approximation was used as shown in Eq. (6). Although (Krishnani and Basu, 2016) suggested that the Boussinesq approximation might bring about substantial changes in flow dynamics, preliminary tests for our proposed study found that the explicit use of a state equation (such as IAPWS-IF97) did not lead to significant alterations in the simulation results. Instead, the explicit incorporation of the source term with density only resulted in a notable increase in computational time, with the model's temperature responses remaining largely unaffected.

$$S_M = -\rho_{ref} \cdot \beta \cdot g_i \cdot (T - T_{ref}) \tag{6}$$

The transport properties of the fluid are considered temperature dependent ($\mu = f(T)$, $K = f(T)$, and $\rho = f(T)$) at a constant pressure of 101325 Pa (atmospheric pressure) plus the hydrostatic contribution due to the expansion tank.

Although the complete geometry of the butterfly valve was not explicitly considered, to account for the pressure drop in this device, porous media were used with a constant resistance loss coefficient ($k_{eq} = 1.12$), which was experimentally determined by the valve manufacturer.

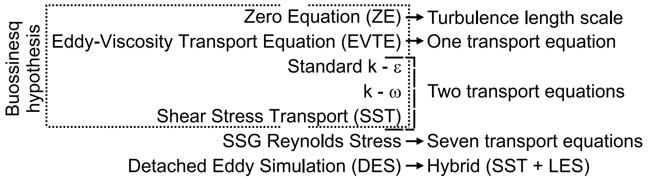

**Fig. 5.** Indication of the turbulence models, conservation equations characteristics and assumed hypothesis.

The flow was considered turbulent, and it was necessary to use a turbulence model. Although several mathematical turbulence models are reported in the literature, their use is intrinsically linked to the physical behavior of a given engineering problem.

The authors recognize that the fluid flow starts as laminar, but at some point, it transitions to a turbulent state. This transition's precise timing and location are inherently uncertain, and the model must incorporate cutoff functions to capture this behavior. In an industrial setting, such as in reactors with intricate geometries, it is imperative to identify which of the available models can most accurately predict this behavior, even with initially laminar flow.

For all the tested turbulence models, the following hypotheses were considered: (i) incompressible fluid, (ii) Newtonian fluid, (iii) negligible variations in the thermodynamic/thermophysical properties due to pressure dependency, (iv) Stoke's hypothesis for the second viscosity coefficient ($\lambda = -(2/3)\mu$), and (v) negligible influence of the viscous dissipation terms in the energy conservation equation.

In this article, the following turbulence models are considered: (i) Zero-equation model (CFX-Solver ANSYS, 2006), (ii) Eddy-viscosity transport equation (Menter and Ames Research Center, 1994; Menter, 1997), (iii) Standard $k-\varepsilon$ model (Launder and Sharma, 1974), (iv) $k-\omega$ model (Wilcox et al., 1998), (v) Shear Stress Transport model (Menter, 1994), (vi) SSG Reynolds Stress model (Speziale et al., 1991), and (vii) Detached Eddy Simulation turbulence model. Notably, these models have been used in their standard form, without any modifications to their constants, so that future studies can benefit from the analysis of the original model. Complete details of the turbulence equations and constants are provided in the Appendix.

Fig. 5 presents the assumptions for each turbulence model proposed in this article. Most of these models incorporate time averaging in the conservation equations and employ the Boussinesq approximation for the Reynolds stresses (Eq. (A.4)).

### *3.1. Spatial discretization*

Before presenting the discretization results, some simplifications were made to the geometry of the heat exchanger to reduce computational demand. The helical geometry was replaced with toroids having the exact dimensions, pitch, and heat transfer area (Fig. 6). This simplification enabled the adoption of a transverse symmetry across the entire loop ($zy$ plane boundary condition), a procedure also performed by Angelo et al. (2012). The computational domain was subsequently divided into two regions, with the heat exchanger region consisting predominantly of hexahedral elements and all other regions containing tetrahedral and prismatic elements.

The methodology employed to verify the spatial and temporal discretization in this article adhered to the process proposed by Stern et al. (2001) and Wilson et al. (2001). This approach involves a successive process of solutions and refinements to minimize errors arising from spatial and temporal discretization.

The steady-state condition was achieved for heater 1, operating at a nominal power of 1000 W (experimental data 1025.4 ± 19.9 W), using a transient simulation continued until the results exhibited no significant variation with time. Upon reaching steady-state, the quantities obtained from the simulation were time-averaged. The values presented

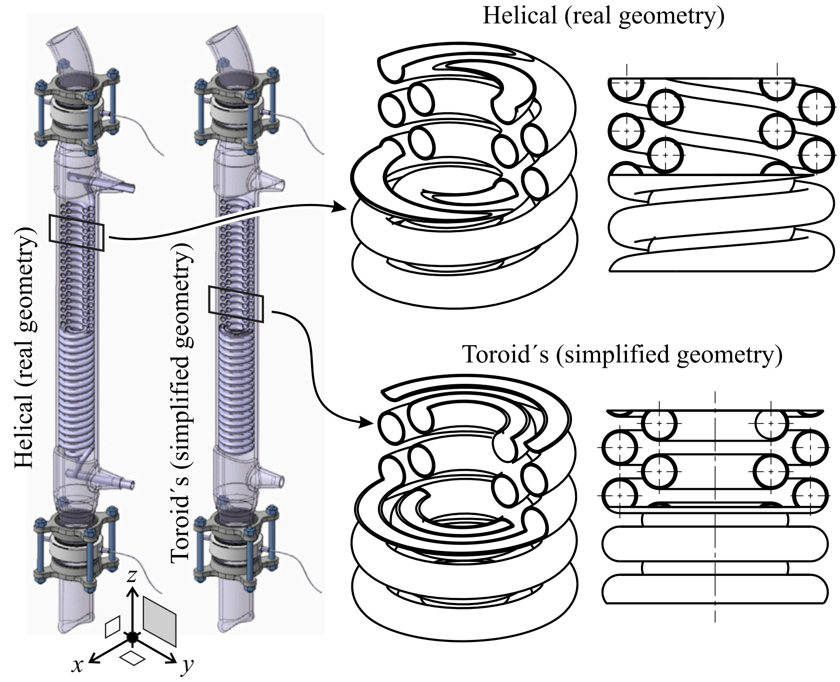

**Fig. 6.** Detail view of geometric simplification.

in the numerical results section of the spatial discretization analysis are these time-averaged quantities.

Although the study was conducted for all turbulence models, the spatial discretization was determined by the most demanding turbulence model and subsequently applied to the others. The DES model required the highest level of spatial discretization. The results of the spatial discretization were obtained for a point near the heater and a point in the vicinity of the heat exchanger, with the average velocity in the $z$-direction ($\bar{u}3$), average temperature ($\bar{T}$), and mean strain-rate tensor ($\overline{S}ij$ - Eq. (A.9)) obtained for each point. Fig. 7 illustrates the position of the points. While the variables analyzed in this study were chosen at specific locations, the overall behavior of the circuit is well represented by these spatial locations (points 1 and 2). As a result, the findings from these regions can be considered representative of the natural circulation loop.

The influence of the number of elements on the average velocity in the $z$-direction, average temperature, and mean strain-rate tensor is illustrated in Fig. 8 for the heater region (point 1) and Fig. 9 for the heat exchanger region (point 2).

Upon analyzing Figs. 8 and 9, a slight divergence between the last two obtained meshes (MA and MB) can be observed. However, for all analyzed quantities, the deviation between the two meshes does not exceed 0.4%. Due to the relatively small deviations, the MA and MB meshes (depicted in Figs. 8 and 9) were used in the simulations to reduce computational time. The total number of elements in the computational domain is approximately 4.31 million.

The Eq. (7) elucidates the method used to determine the $y^+$ value in our study. At any given time and for any coordinate close to the wall, $y^+$ remains below 0.91 across all turbulence models. This low $y^+$ value ensures that if feasible, the model can compute even the viscous sublayer behavior. However, for the Eddy-Viscosity Transport Equation (EVTE), Standard $k-\varepsilon$ model, and SSG Reynolds Stress turbulence model, they do not leverage this low $y^+$ advantage due to the unalterable characteristic of Ansys CFX which enforces the logarithmic wall law regardless of the near-wall discretization.

$$y^+ = \frac{\rho}{\mu}\delta y\sqrt{\frac{\tau_p}{\rho}} \tag{7}$$

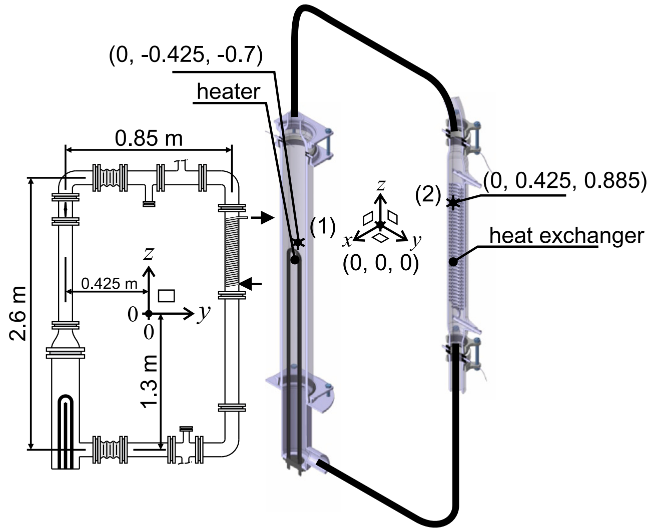

**Fig. 7.** Schematic of the experimental apparatus, indicating the positions of points 1 and 2 for spatial discretization verification.

### 3.2. Temporal discretization

The procedure for determining the time step in the transient solution followed a methodology analogous to that described for spatial discretization. However, an adaptive time scale was employed as a function of the maximum Courant number (Equation 6) throughout the entire computational domain.

$$Co_{max} = \Delta t\left(\frac{\overline{U}_{i_{max}}}{\Delta l_{min}}\right)_{max} \tag{8}$$

Here, $\Delta t$ represents the time step, and $\left(\frac{\overline{U}imax}{\Delta l_{min}}\right)max$ is obtained for a given volume that yields the maximum average velocity in any direction ($\overline{U}i_{max}$) divided by the smallest volume edge length ($\Delta l_{min}$).

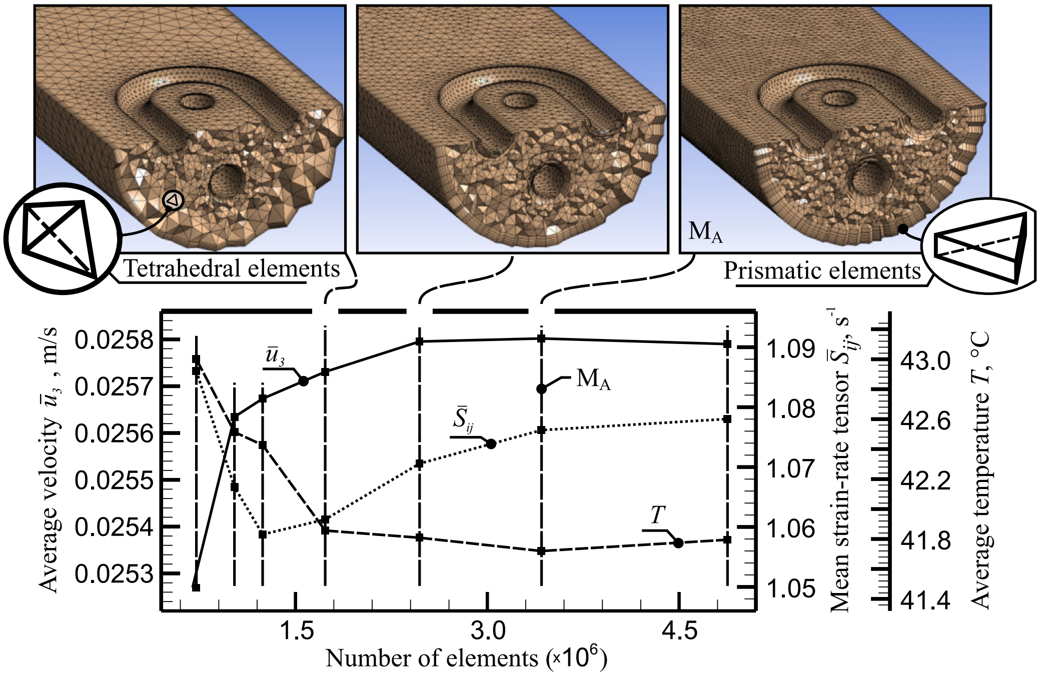

**Fig. 8.** Point 1 - Influence of the number of elements on the average velocity, average temperature, and mean strain-rate tensor under steady-state conditions for a nominal power of 1000 W in heater 1.

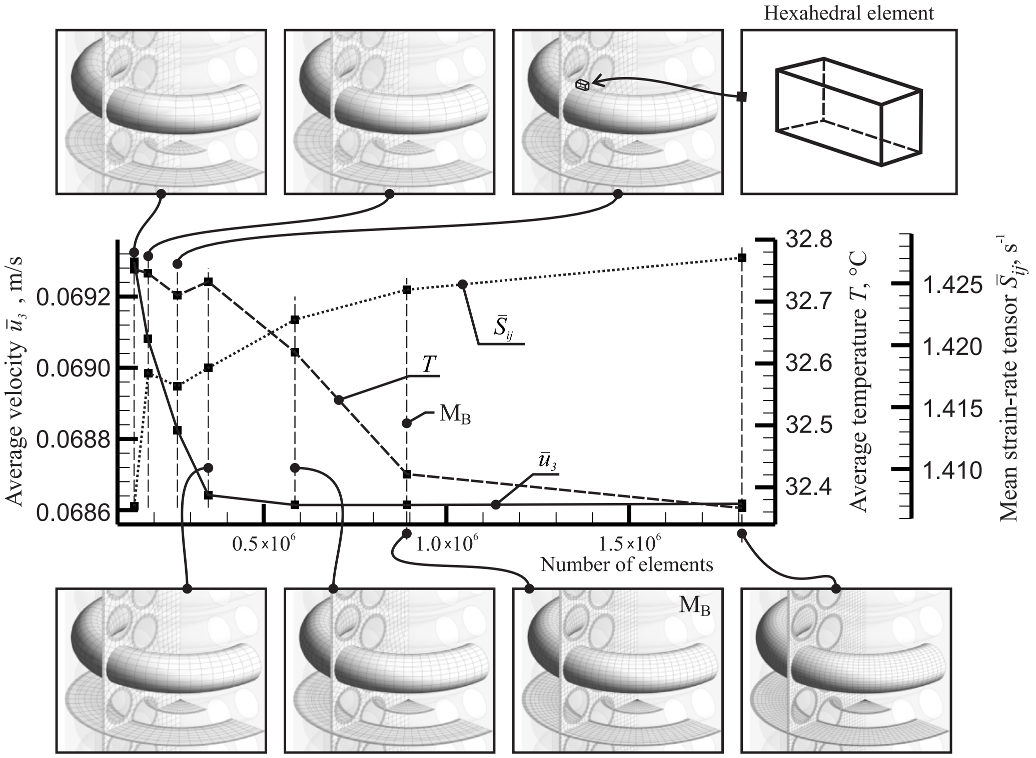

**Fig. 9.** Point 2 - Influence of the number of elements on the average velocity, average temperature, and mean strain-rate tensor under steady-state conditions for a nominal power of 1000 W in heater 1.

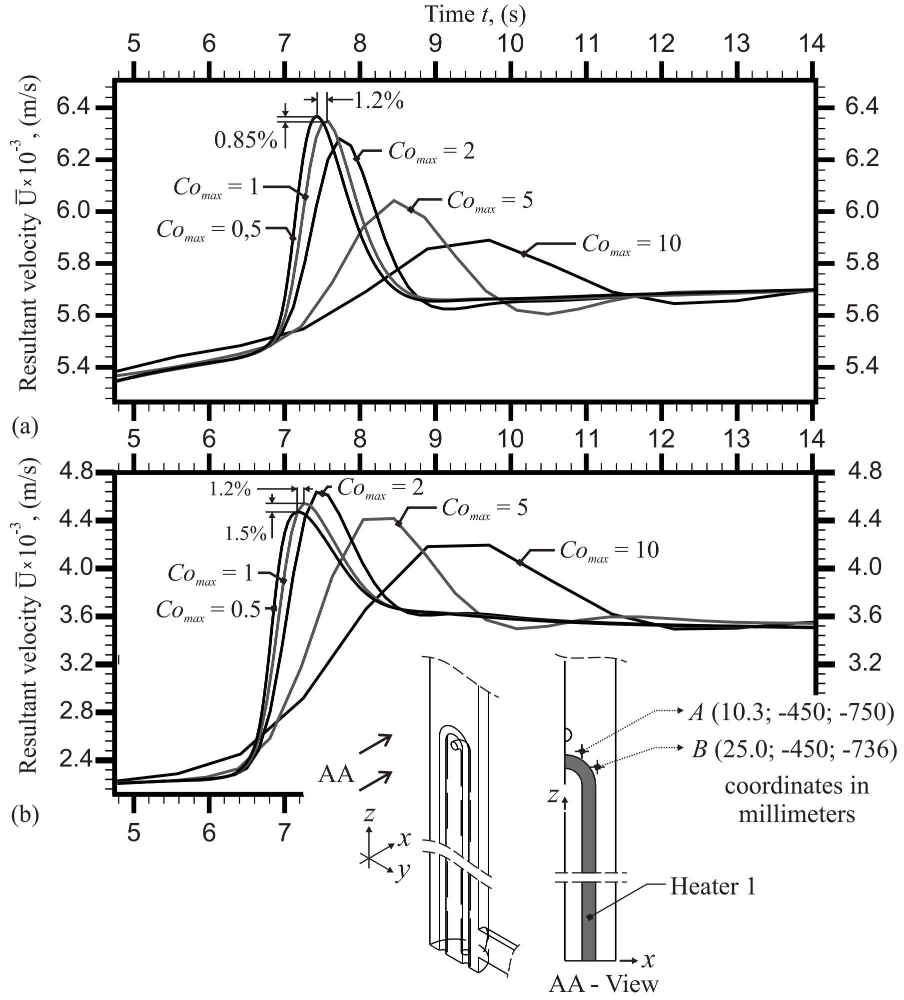

**Fig. 10.** (a) Verification of the influence of maximum Courant number on the velocity (U) as a function of time at point A with coordinates (10.3 mm, -450 mm, -750 mm). (b) Verification of the influence of maximum Courant number on the velocity (U) as a function of time at point B with coordinates (25 mm, -450 mm, -736 mm).

The adaptive method calculates the maximum Courant number for the entire computational domain after each time step. If this maximum value exceeds or falls below a predetermined threshold, the time step is adjusted accordingly, and the process repeats until the desired threshold is achieved. This approach enables the method to dynamically adapt to the changing conditions of the simulation, ensuring accurate results.

To determine the appropriate maximum Courant number, multiple simulations were conducted, with the maximum Courant number gradually decreasing in successive simulations until no substantial changes were observed. Since the DES turbulence model typically requires the shortest time step (Sagaut, 2006) among the models studied, it was employed to determine the maximum Courant number that would be applied to all other turbulence models in this study.

To study the variation in the velocity field and assess the potential influence of the maximum Courant number on temporal discretization, two arbitrary points near heater 1, labeled A and B, were selected. Figs. 10a and 10b display the variation in velocity (U) at these points as a function of time over a 5 to a 14-second interval, with the chosen points corresponding to a region where significant variation in the velocity field.

A maximum Courant number of 1 was adopted as the standard for all simulations. The maximum deviation in the monitored velocity (U) between simulations with $Co_{max}$ = 1 and $Co_{max}$ = 0.5 did not exceed 1.5% throughout the analysis. Although the authors acknowledge that a maximum deviation of 1.5% is relatively high, employing $Co_{max}$ = 0.5 would lead to simulations with excessively long computational times, rendering it impractical for the scope of this study.

### 3.3. Solver configuration

In this study, consistent solver settings were prioritized across all analyses, where feasible. This section summarizes the computational strategies employed, reiterating key specifics previously introduced for clarity. Below, the discretization schemes and solver configurations selected for this investigation are detailed:

1. **Time-Discretization Scheme:** The Second-Order Backward Euler scheme was employed for all simulations.
2. **Advection Scheme:** For advection terms, the High-Resolution scheme was utilized. Distinctively, the Detached Eddy Simulation (DES) model employs the Central Differencing scheme due to its LES-based formulation.
3. **Convergence Criteria:** All simulations were configured to achieve convergence with maximum normalized residuals less than $1 \times 10^{-5}$.
4. **Time-Stepping Strategy:** An adaptive time-stepping approach, determined by the maximum Courant number, was applied. This method, which dynamically adjusts time steps for computational (Section 3.2).
5. **Wall Treatment:**
    - The Zero Equation model did not require the application of wall functions.

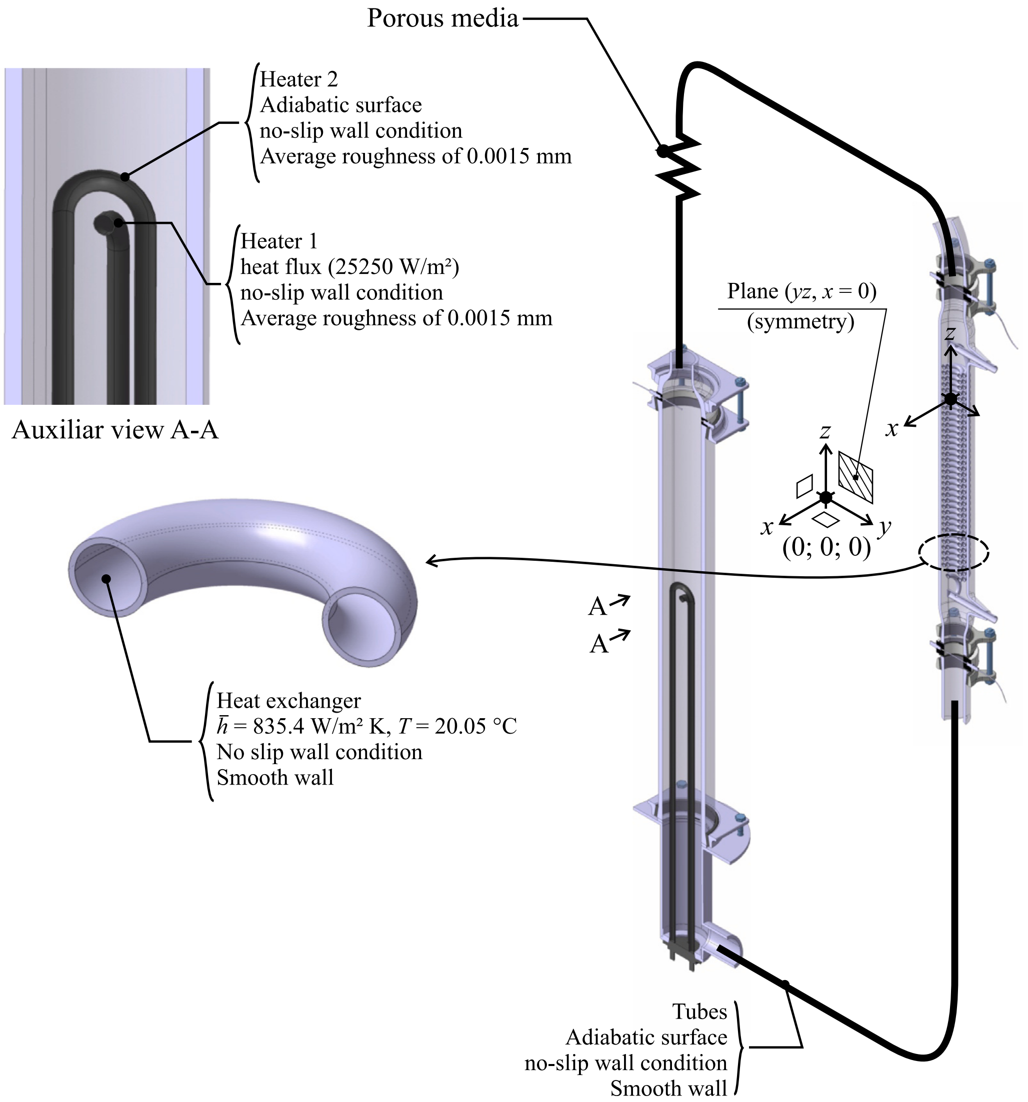

**Fig. 11.** Schematic representation of boundary conditions.

- For the Eddy Viscosity Transport Equation (EVTE), $k - \varepsilon$, and the Reynolds Stress (SSG), a wall function based on the standard logarithmic profile was used.
- The $k{-}\omega$, Shear Stress Transport (SST), and Detached Eddy Simulation (DES) models employ a Low-Reynolds number formulation for near-wall treatment.

### 3.4. Boundary conditions

The boundary conditions used in the model are shown in Fig. 11. The following are the descriptions and considerations:

1. Temperature variations inside the helical tubes of the heat exchanger were considered negligible due to the high fluid flow rate, and the average temperature of the fluid inside the tubes was taken as 20.05 °C;
2. The heat transfer coefficient for the inner surface of the heat exchanger tubes, corresponding to the forced flow within the helix, was computed taking into account the conductive resistance of the glass, with an approximate thickness of 1 mm, and the internal convective coefficient based on the correlation proposed by Rogers and Mayhew (1964). Consequently, this derived convective coefficient, applied to the heat exchanger's inner surface, is 835.4 W/m$^2$ K.;
3. Heat transfer in heater 1 was determined to be 1025.4 W, which corresponds to a heat flux of 25 891 W/m$^2$;
4. No-slip wall, smooth wall conditions were applied to all surfaces;
5. Heat exchange with the external environment through the glass via conduction and natural convection external to the glass tubes was neglected;
6. The entire domain was considered symmetrical in the $yz$ plane (Fig. 11);
7. The pressure loss caused by the butterfly valve was simulated using a dedicated computational region modeled as a porous medium. This approach employed a head loss coefficient of 1.12, as specified by the valve manufacturer. This coefficient was applied across a subdomain with a total length of 100 mm, resulting in a calculated resistance loss coefficient of 11.2 m$^{-1}$. The porous medium used in the simulation was assumed to be isotropic, and its porosity was set to 1.

At the start of the simulation, the fluid within the computational domain was assigned an initial temperature of 20.05 °C and no initial velocity ($u_i$).

The glass tube surfaces were considered adiabatic due to their low thermal conductivity (1.15 $\frac{\mathrm{W}}{\mathrm{m\ K}}$) and significant thickness (4.4 mm), resulting in high conduction resistance. Natural convection on the external surfaces also contributed to low temperatures, considerably

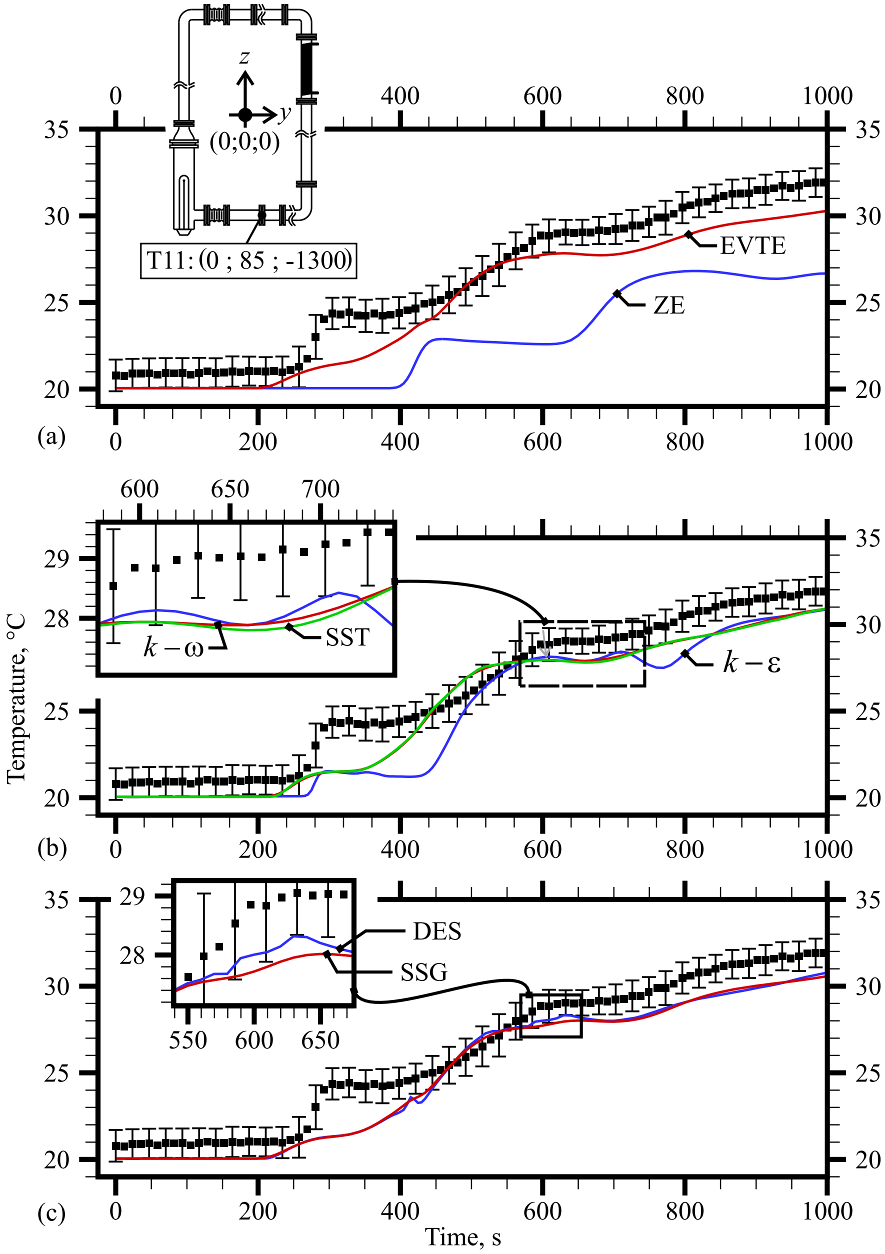

**Fig. 12.** Time-dependent comparison of the numerical solution and experimental measurements for thermocouple T11.

reducing the average convective coefficient. This combination of factors resulted in high total thermal resistance, minimizing heat exchange with the surrounding environment.

In the steady-state regime, heat exchange with the environment was maximized. Analyzing the data from thermocouples T21 and T22 (which measured the cold fluid temperature in the exchanger), the energy transferred was approximately 1007 W. Since the NCL operated at a nominal power of 1025 W, the omission of environmental loss resulted in an error of approximately 2%.

### 3.5. Results

The results were analyzed by directly comparing the numerical and experimental temperature measurements obtained at each thermocouple location and time.

Under the experimental conditions discussed, the steady-state regime was established around three thousand seconds after the phenomenon's onset, as indicated in Fig. 4. However, the most significant variations occurred within the first one thousand seconds, particularly the large fluctuations in the measured temperature values. For this reason, Figs. 12 to 18 display the temporal variation of temperature results for each of the thermocouple positions obtained in each of the seven tested turbulence models, as well as the experimental readings, up to a time of 1000 s.

Including all simulation data for the turbulence models and the experimental measurements resulted in significant visual clutter. Consequently, we divided Figs. 12 to 18 into three diagrams with a maximum of four distributions per graph. Additionally, each of the mentioned figures contains a small, detailed drawing indicating the thermocouple installation point and its coordinates within a global Cartesian coordinate system. All points are located precisely at the center of the glass tubes, corresponding to the actual position of the natural circulation loop thermocouple at the junction, as depicted in Figs. 3 and 4.

A detailed analysis of the graphs indicated that, in general, the overall macroscopic behavior of temperature was captured in all simulations except for the Zero Equation model. However, some models

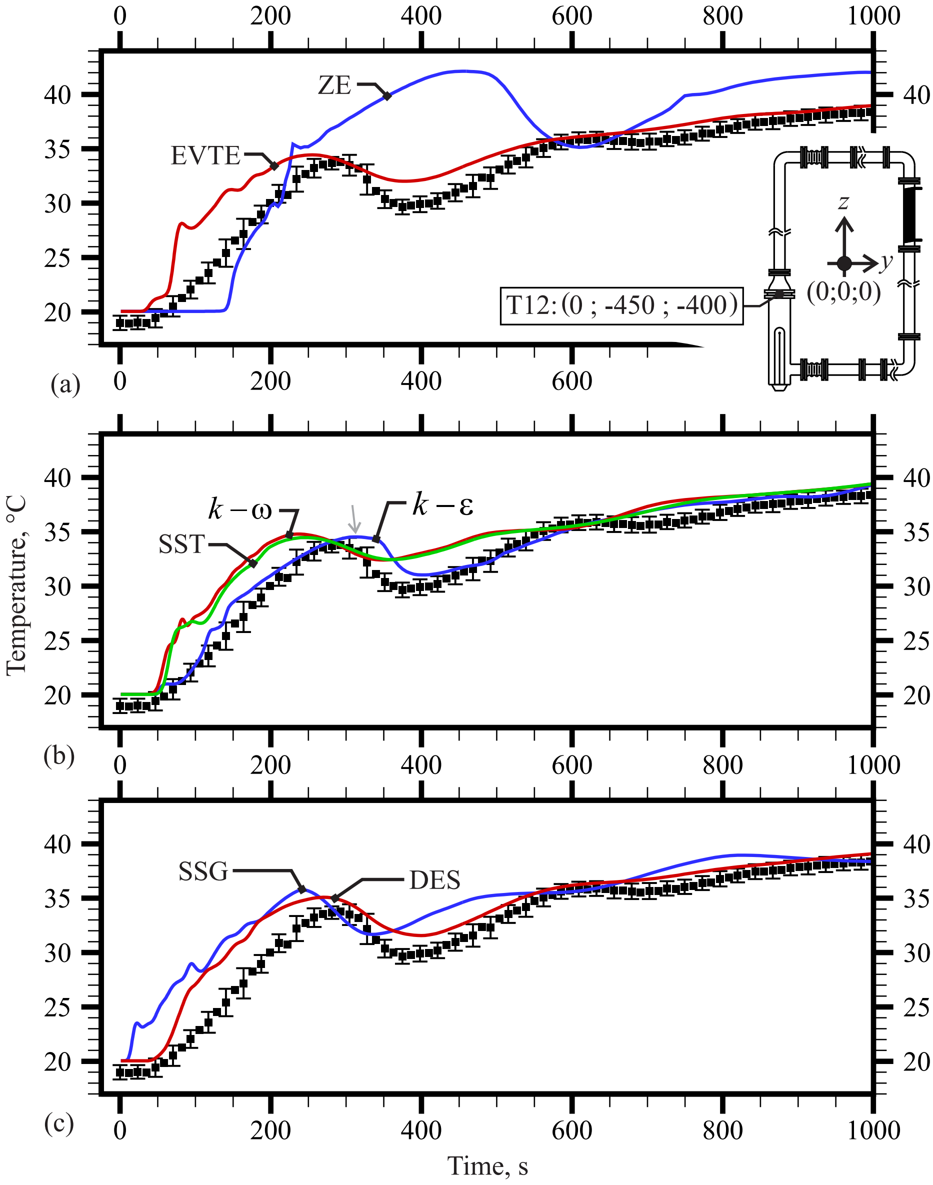

**Fig. 13.** Time-dependent comparison of the numerical solution and experimental measurements for thermocouple T12.

also exhibited relatively high deviations compared to the experiments in certain instances. A temporal differentiation was performed to identify the best model for predicting the phenomenon. A deviation was established for each time interval to the experimental measurement, according to Eq. (9). The determination of the deviation was limited by the temporal information of the data acquisition system (10 s), as the adaptive time steps were much smaller ($6\times10^{-5}$ to 0.1 s) than the experimental readings.

$$\mathrm{dev}_{\%} = \frac{\left|T_N(t) - T_{\exp}(t)\right|}{T_{\exp}(t)} \cdot 100 \tag{9}$$

Where $T_N(t)$ is the fluid temperature obtained through computational simulation at a specific position and instant, $T_{exp}(t)$ is the temperature obtained through measurements at the same position and instant.

The deviations can be analyzed in Fig. 19, constructed for thermocouple number 12 (heater region) as an example for deviation analysis. Thermocouple 12 was chosen among the monitored positions because it exhibited the highest thermal amplitude until the steady-state condition was reached. It qualitatively represents the other monitored positions.

Disregarding the results of the zero-equation model, which exhibited excessively high deviations, the largest deviations for the other turbulence models occurred at the beginning of the transient process (within the first 200 s). Following this period, the deviations tended to decrease significantly over time.

In Fig. 20, the highest deviation (Eq. (10)) obtained between the numerical and experimental solutions among the eight sensors for each turbulence model, the mean deviation (the average of deviations obtained over time (Eq. (11))), and the standard deviation (Eq. (12)) are shown for the monitored positions based on the readings of the eight thermocouples available for comparison up to 1000 s.

$$dev_{max_{\%}} = \max_{i \in n} dev_{\%}(i) \tag{10}$$

$$\overline{dev_{\%}} = \frac{1}{n}\sum_{i=0}^{n} dev_{\%}(i) \tag{11}$$

$$\sigma_{dev} = \frac{1}{n}\sum_{i=0}^{n}\left(dev_{\%}(i) - \overline{dev_{\%}}\right)^2 \tag{12}$$

By considering both the lowest maximum deviation and average deviation simultaneously, the $k-\varepsilon$ model and the DES model stand out as having good performance among the tested models. The zero-equation model (ZE) yielded the worst results and was discarded based

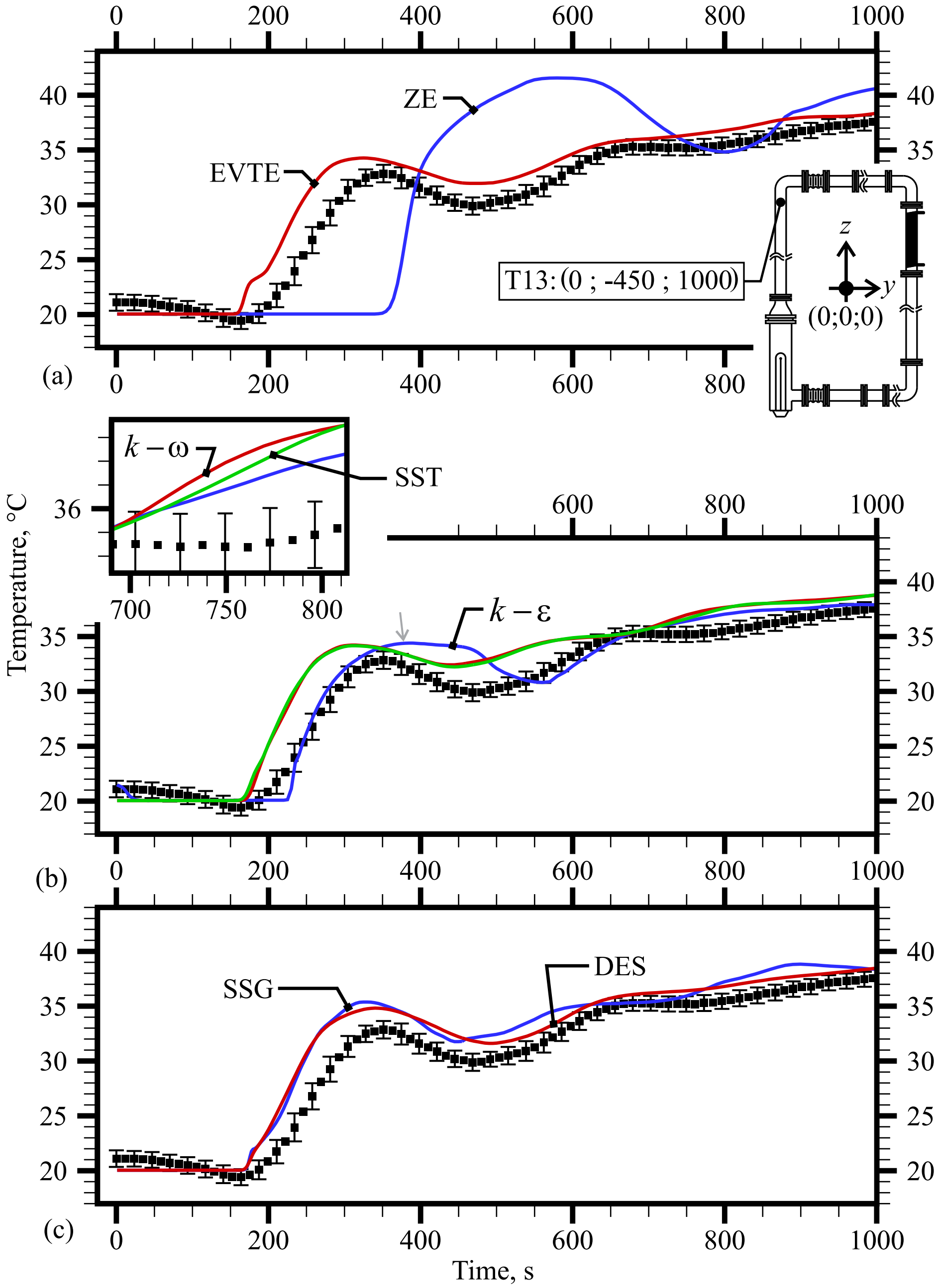

**Fig. 14.** Time-dependent comparison of the numerical solution and experimental measurements for thermocouple T13.

on this criterion for the application in question. The responses of the other turbulence models (EVTE, $k-\omega$, SST, and SSG) on the same comparative basis exhibited very similar trends.

However, even though the DES model has a higher maximum deviation and average deviation compared to the $k-\varepsilon$ model, it is essential to note that the qualitative behavior of temperature variations over time, as analyzed through the shape of the curves (figures from 12 to 18), is relatively well captured by the DES model, except for a noticeable advancement in temperature values.

Another important observation is that no model accurately captured abrupt temperature changes such as those presented by thermocouples T11 (Fig. 12) at 280 s, T17 (Fig. 17) at 90 s, and T18 (Fig. 18) at 220 s.

The natural circulation circuit experiences transient flow that starts from a static condition, where initially, no turbulence is observed. As convective currents intensify over time, turbulence grows. However, in the early stages, some models (EVTE, $k-\omega$, SST, DES, SSG) exhibited non-existent fluctuations in the quantities, which were quickly amplified. This mismatch of fluctuations, at least in the initial stages, contributed to the intensification of convective heat transfer, significantly impacting the development of the temporal solution.

As evidence supporting this observation, two representative quantities were chosen to verify the variation of turbulent quantities, specifically the production terms related to buoyancy: $P_k$ (Eq. (A.21)) and $P_{kb}$ (Eq. (A.22)). $P_k$ is the term responsible for producing turbulence kinetic energy, while $P_{kb}$ represents the contribution of buoyancy to turbulent kinetic energy. These two quantities are shown in Figs. 21 and 22, respectively, as a function of time for the average values obtained along a line for the EVTE, $k-\varepsilon$, $k-\omega$, SST, DES, and SSG models. It is important to note that not all turbulence models perform explicit accounting of these production terms; in these models, quantities are calculated after simulation and determined in post-processing. The values are obtained at discrete points along a line positioned immediately downstream of

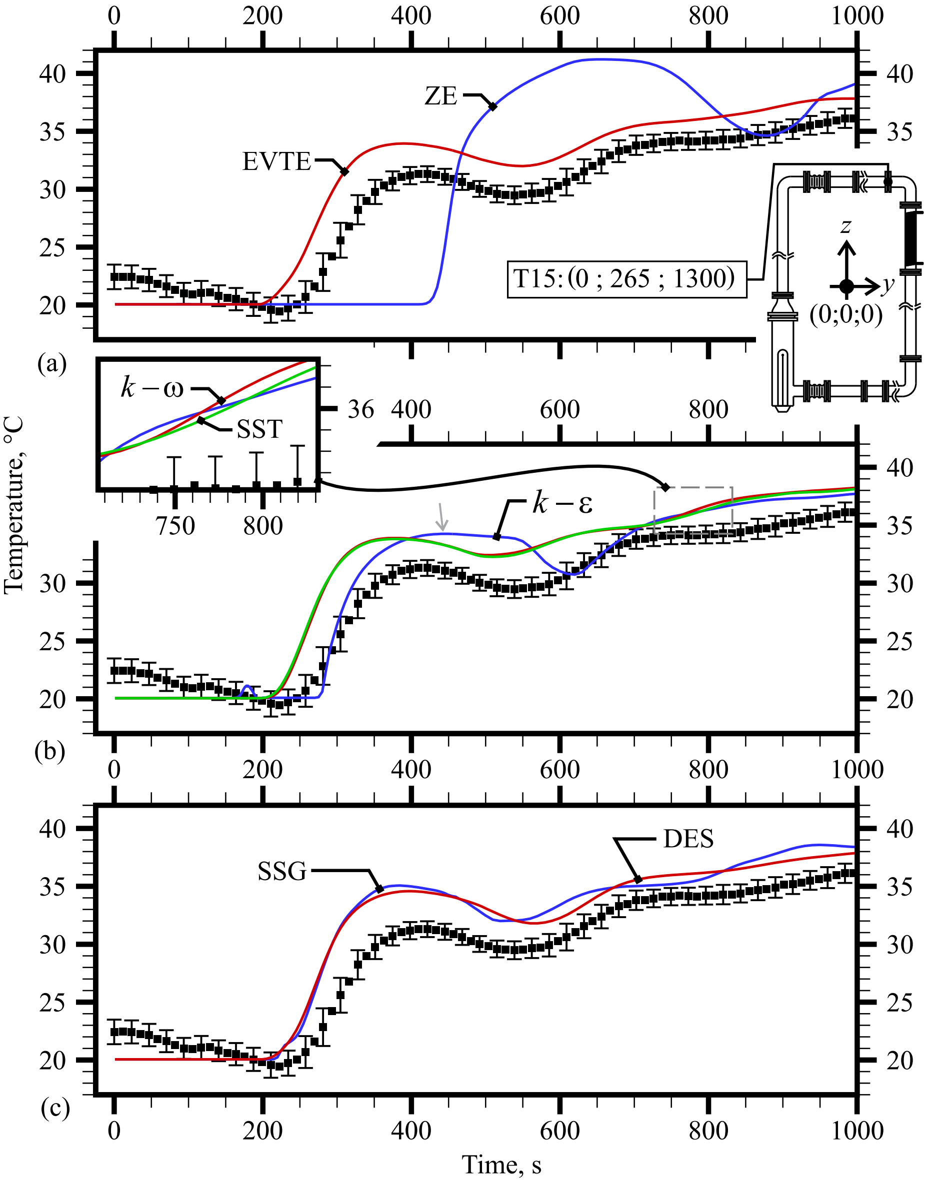

**Fig. 15.** Time-dependent comparison of the numerical solution and experimental measurements for thermocouple T15.

the heater region, which is the primary source of convective currents in the system, and then averaged to obtain a mean value.

Analysis of Fig. 21 reveals that the $P_k$ term has its lowest value in the early stages for the $k-\varepsilon$ model. In contrast, all other models show values one or two orders of magnitude higher, with high turbulence production for at least the first 40 s. Furthermore, Fig. 22 shows that the models (EVTE, $k-\omega$, SST, DES, SSG) overestimate the flow temperature after the heat exchanger due to this effect, influencing the entire circuit. Therefore, it can be concluded that these models numerically intensify convective currents.

The trend observed for $P_k$ is replicated for $P_{kb}$ in Fig. 22, except for the SSG model, which initially shows low values for the quantity. However, the quantity also undergoes a significant increase in the first few seconds for the SSG model.

In Fig. 23, the average value of the product $\overline{u'_3u'_3}$ is presented for the EVTE, $k-\varepsilon$, $k-\omega$, SST, SSG, and DES models. This plot shows the average intensity of velocity fluctuations in the vertical direction ($z$-axis) over time during the initial stages of the simulation (up to 100 s). These results confirm the earlier assertion that turbulent quantities are consistently higher in the initial stages for all models, except for the $k-\varepsilon$ model.

A study conducted by Walsh and Leong (2004) compared the performance of three turbulence models ($k-\varepsilon$, RNG $k-\varepsilon$ and SSG) for natural convection in cubic cavities filled with air under low turbulence conditions. The results indicated that the $k-\varepsilon$ model was the most efficient among the three models. In the initial stages of natural circulation flows, the flow is often characterized by low or nonexistent turbulence, and the $k-\varepsilon$ model is better suited for accurately capturing this flow behavior. Therefore, this model is recommended for simulating the initial stages of natural circulation flows.

The observation of temperature variations in the experimental data showed that the anticipation of these variations could have been better captured by the EVTE, $k-\omega$, SST, DES, and SSG turbulence models, as verified at all experimental monitoring points. The results were uneven, indicating that this is not a mathematically linear phenomenon. It is insufficient to adjust the temperature over time (in these models) for all points in the circuit by shifting the curves in time by a fixed value. In contrast, in the $k-\varepsilon$ model, the production of numerical fluctuations is lower, as evidenced by the lower average deviation over time from zero to one thousand seconds.

Although the $k-\varepsilon$ model produces smaller deviations, it appears to be less sensitive in capturing temperature decreases, as can be seen

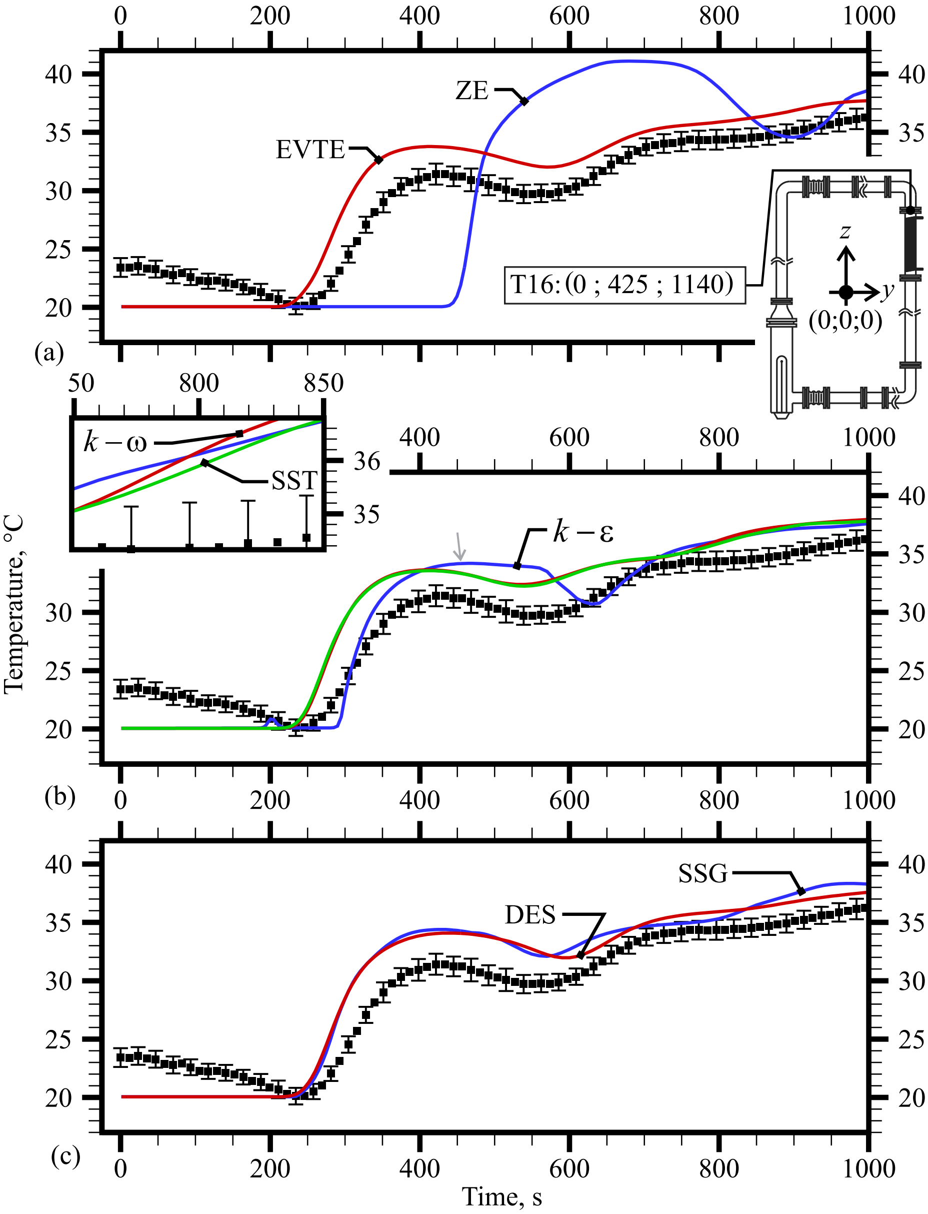

**Fig. 16.** Time-dependent comparison of the numerical solution and experimental measurements for thermocouple T16.

in the regions indicated by gray arrows in Figs. 13, 14, 15, and 16. Compared to the other models, the $k-\varepsilon$ model exhibits lower turbulence energy dissipation, which also contributes to the delay in the onset of temperature decrease.

In Fig. 24, the flow in the heater region, obtained from the steady-state solution of the DES model, is presented. Fig. 24a shows the streamlines and details of recirculation regions on the $xz$ plane.

In this research, the identification of vortex structures was based on the Q criterion, as established by Kolář (2011). This criterion delineates vortex as regions wherein the second invariant of the velocity gradient tensor is positive, as calculated according to Eq. (13).

$$Q' = \left[\left(\frac{\partial \bar{U}_i}{\partial x_j}\right)^2 - \frac{\partial \bar{U}_i}{\partial x_j}\frac{\partial \bar{U}_j}{\partial x_i}\right] = \bar{\Omega}_{ij}^2 - \bar{S}_{ij}^2 \qquad (13)$$

Fig. 24 displays an isosurface for the quantity $Q' = 0.01, s^{-2}$, with vortex centers located inside the regions delimited by this surface. Among other details, this representation reveals areas of intense turbulence at the heat exchanger entrance, generated by the inlet geometry. Furthermore, Fig. 24b distinguishes three regions: the lower portion featuring large vortices, the intermediate region with small vortices, and the upper heater region with larger recirculations.

## 4. Conclusions

A numerical study of the vertical heater, vertical cooler (VHVC) natural circulation loop (NCL) at IPEN/CNEN-SP was carried out. The mathematical model employed was three-dimensional and transient, analyzed using the commercial software ANSYS CFX. The spatial and temporal discretization verification was thoroughly examined, utilizing techniques recommended in the literature.

Seven turbulence models were employed: Zero Equation, Eddy Viscosity Transport Equation (EVTE), $k-\omega$, $k-\varepsilon$, Shear Stress Transport (SST), Reynolds Stress (SSG), and Detached Eddy Simulation (DES). The results of the models were compared against each other, as well as against experimental results obtained specifically for this purpose. Due to the characteristics of the experiment, the comparisons primarily focused on the spatial distribution and temporal evolution of temperature at various points in the natural circulation circuit.

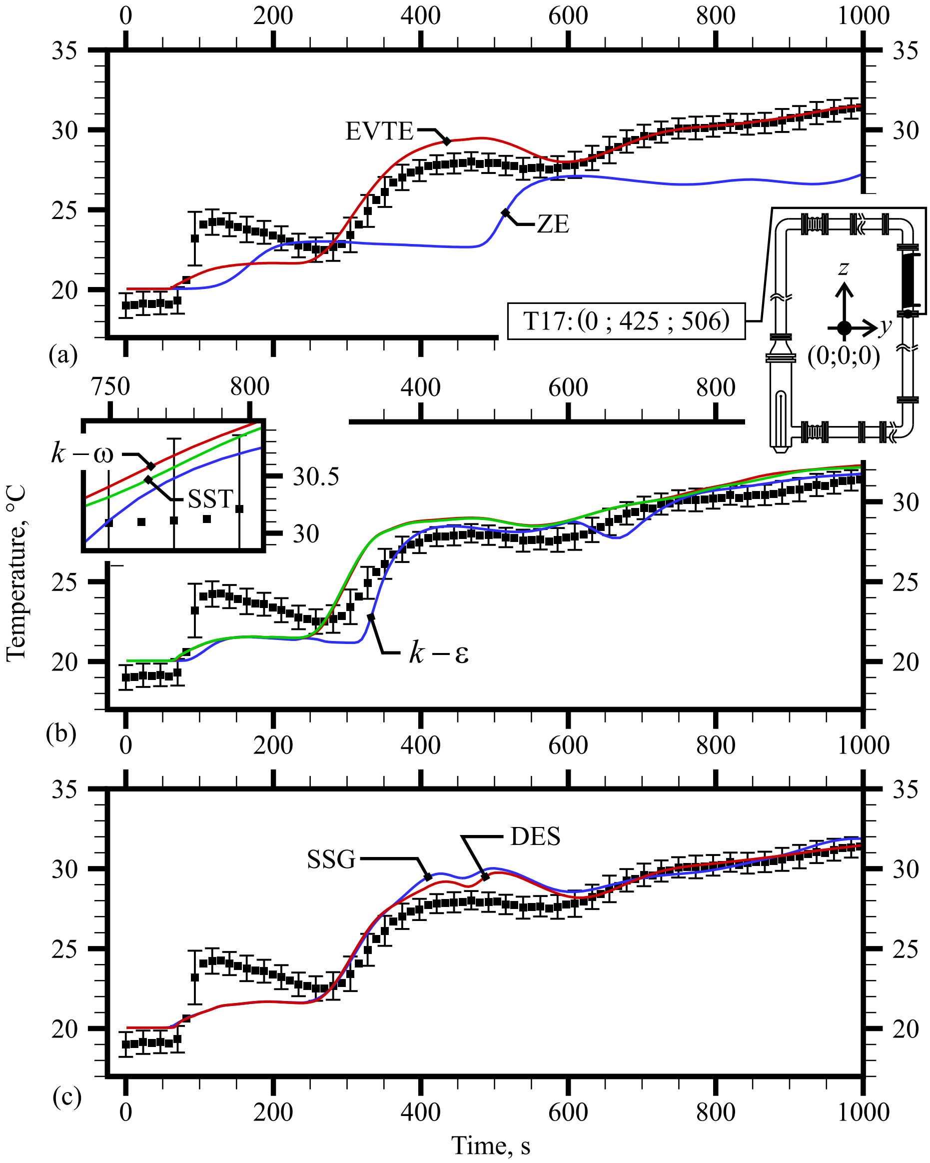

**Fig. 17.** Time-dependent comparison of the numerical solution and experimental measurements for thermocouple T17.

The study found that for the 1000 W heater's nominal power, the transient flow lasted around 3000 s, with the most notable fluctuations in quantities occurring within the first 1000 s. Consequently, the time interval from the onset of natural circulation with a zero temperature gradient to 1000 s was selected to compare the transient results of the analyzed turbulence models.

The Zero Equation model displayed significant deviations when comparing temperature results obtained from each turbulence model at instrumented points in the experimental circuit under transient conditions. In contrast, the EVTE, $k-\omega$, SST, SSG, and DES models exhibited intermediate deviations. The $k-\varepsilon$ model, on the other hand, demonstrated superior performance, with the lowest average deviation among all tested models.

The $k-\varepsilon$ model exhibited lower initial turbulence production than the more complex models, leading to a smaller deviation in temperature estimates. The EVTE, $k-\omega$, SST, and SSG models were significantly more affected by initial turbulent quantities, while the DES model was also impacted, although less noticeably. This behavior suggests that the $k-\varepsilon$ model is more accurate in predicting temperature distribution and is a better choice for transient flow analysis in the natural circulation loop.

While various turbulence models were tested and compared with experiments, only one operating power was utilized (1000 W). The authors acknowledge that varying the applied power of the NCL for different conditions could provide a more comprehensive validation of the mathematical model. However, it is noted that in stable conditions and without phase change, the behavior of the NCL appears consistent, with differences manifesting primarily in temperature amplitudes. Given that the study explored a range of Rayleigh numbers (0 to $2.8\times10^8$), it suggests that the k-epsilon model may offer promising results compared to the experiments within this spectrum.

Another factor that must be addressed is the computational resource requirement, stemming from two main aspects: the processing time due to the small time step (initially 1E−7 s and being incremented according to the Courant number), and the need for data storage. These factors make post-processing challenging.

In the continuation of this research, efforts are directed at obtaining a system to measure the velocity field near the electrical resistance. Studies are being conducted to identify the best method to achieve this objective. Although temperature measurements provide insight into general behavior, they might not capture detailed flow dynamics. Therefore, adding velocity field measurements is expected to offer a more detailed understanding of the phenomena.

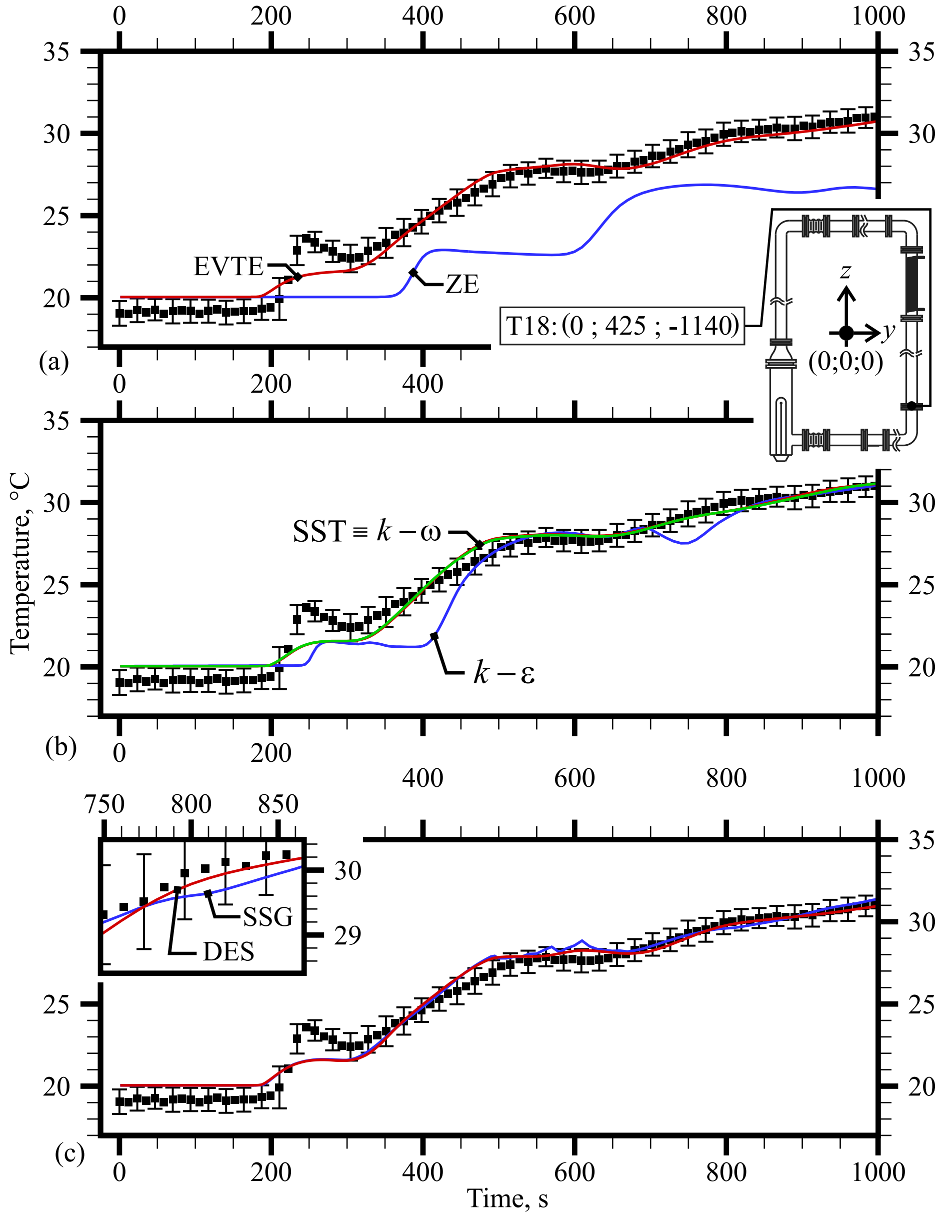

**Fig. 18.** Time-dependent comparison of the numerical solution and experimental measurements for thermocouple T18.

## CRediT authorship contribution statement

**G. Angelo:** Writing – review & editing, Writing – original draft, Visualization, Validation, Software, Methodology, Investigation, Formal analysis, Data curation, Conceptualization. **E. Angelo:** Methodology, Formal analysis, Data curation, Conceptualization. **N.L. Scuro:** Writing – original draft, Resources, Data curation. **W.M. Torres:** Resources, Investigation, Data curation. **D.A. Andrade:** Writing – review & editing, Writing – original draft, Supervision, Software, Methodology, Formal analysis, Data curation, Conceptualization.

## Declaration of competing interest

The authors declare the following financial interests/personal relationships which may be considered as potential competing interests: Gabriel Angelo reports financial support and administrative support were provided by Mackenzie Presbyterian University. If there are other authors, they declare that they have no known competing financial interests or personal relationships that could have appeared to influence the work reported in this paper.

## Data availability

Data will be made available on request.

## Acknowledgments

This work was partially supported by the Mackenzie Fund for Research and Innovation - MackPesquisa, as well as the Energy and Nuclear Research Institute.

## Appendix A. Reynolds-averaged Navier–Stokes models

The Zero-Equation, Eddy Viscosity Transport Equation (EVTE), $k-\varepsilon$, $k-\omega$, Shear Stress Transport (SST), and SSG turbulence models are all based on the time averaging of conservation equations. The temporal averages for the conservation of mass (A.1), momentum (A.2), and energy (A.3) are presented below.

$$\frac{\partial \bar{U}_i}{\partial x_i} = \frac{\partial u'_i}{\partial x_i} = 0 \tag{A.1}$$

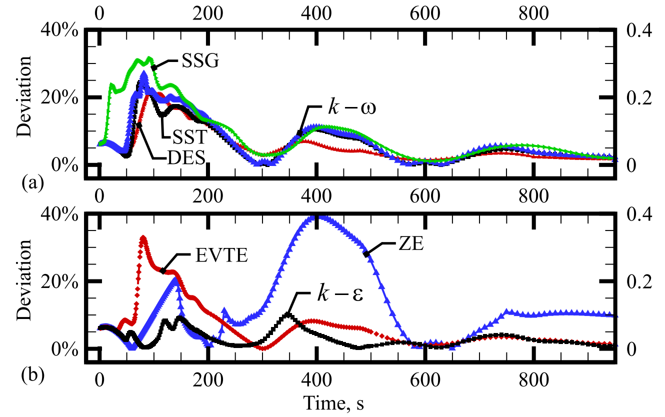

**Fig. 19.** Temperature deviation over time between numerical results and experimental values for position (0; -450; -400) – thermocouple 12 – and models: (a) $k-\omega$, SST, SSG, DES, and (b) ZE, EVTE, $k-\varepsilon$.

$$\rho\frac{\partial\bar{U}_i}{\partial t}+\rho\frac{\partial}{\partial x_i}\bar{U}_i\bar{U}_j=-\frac{\partial\bar{p}}{\partial x_i}+\frac{\partial}{\partial x_j}\left(\mu\left(\frac{\partial\bar{U}_i}{\partial x_j}+\frac{\partial\bar{U}_j}{\partial x_i}\right)-\rho\overline{u'_iu'_j}\right)+\rho_{\mathrm{ref}}\beta(T-T_{\mathrm{ref}})g_i \tag{A.2}$$

$$\frac{\partial\bar{T}}{\partial t}+\frac{\partial}{\partial x_i}\left(\bar{U}_i\bar{T}\right)=\frac{\partial}{\partial x_i}\left(\alpha\frac{\partial\bar{T}}{\partial x_i}-\overline{u'_iT'}\right) \tag{A.3}$$

### *A.1. Turbulent viscosity-based models*

The zero-equation, EVTE, $k-\varepsilon$, $k-\omega$, and SST turbulence models, utilize the Boussinesq approximation. For an incompressible fluid, the turbulent viscosity is defined by (A.4).

$$-\rho\overline{u'_iu'_j}=\mu_t\left(\frac{\partial\bar{U}_i}{\partial x_j}+\frac{\partial\bar{U}j}{\partial x_i}\right)-\frac{2}{3}\delta_{ij}\rho k \tag{A.4}$$

Similarly, for the equation of conservation of energy, the tensor related to the turbulent heat transfer rate $\overline{(u'_i, T')}$ is obtained as indicated in Eq. (A.5).

$$-\overline{u'_jT'}=\frac{\mu_t}{\rho\mathrm{Pr}_t}\frac{\partial\bar{T}}{\partial x_i} \tag{A.5}$$

#### *A.1.1. The zero equation model*

The zero equation model uses an algebraic relationship for the calculation of turbulent viscosity in Eq. (A.6), and assumes the length scale $l_t$ (Eq. (A.7)).

$$\mu_t=\rho\, f_\mu\, U_t\, l_t \tag{A.6}$$

$$l_t=\frac{\sqrt[3]{\forall}}{7} \tag{A.7}$$

#### *A.1.2. One-equation: Eddy viscosity transport model*

The Eddy Viscosity Transport Model includes a transport equation for the turbulent kinematic viscosity (Eq. (A.8)). The constants used in this model are presented in Table A.1. The remaining necessary relationships are presented in Eqs. (A.9) to (A.17).

$$\rho\frac{\partial\nu_t}{\partial t}+\rho\frac{\partial}{\partial x_j}\left(\bar{U}_j\,\nu_t\right)=c_1\,D_1\rho\,\nu_t\overline{S_{ij}}-c_2\rho E_{1e}+\left[\left(\mu+\frac{\rho\nu_t}{\hbar}\right)\frac{\partial\nu_t}{\partial x_j}\right] \tag{A.8}$$

$$\bar{S}_{ij}=\frac{1}{2}\left(\frac{\partial\bar{U}_i}{\partial x_j}+\frac{\partial\bar{U}_j}{\partial x_i}\right) \tag{A.9}$$

$$\tilde{\nu}_t=\frac{\nu_t}{D_2} \tag{A.10}$$

$$D_2=1-e^{-\left(\frac{\tilde{\nu}_t}{A^+\kappa}\right)} \tag{A.11}$$

$$D_1=\frac{\tilde{\nu}_t+\nu}{\nu_t+\nu} \tag{A.12}$$

$$E_{1e}=c_3\,E_{BB}\,\tanh\left(\frac{E_{k-\varepsilon}}{c_3E_{BB}}\right) \tag{A.13}$$

$$E_{k-\varepsilon}=\nu_t^2\left(\frac{1}{L_{\upsilon K}}\right)^2 \tag{A.14}$$

$$E_{BB}=\frac{\partial\nu_t}{\partial x_j}\frac{\partial\nu_t}{\partial x_j} \tag{A.15}$$

$$\left(L_{\upsilon K}\right)^2=\left|\frac{2\bar{S}_{ij}\bar{S}_{ij}}{\frac{\partial\bar{S}_{ij}}{\partial x_j}\frac{\partial\bar{S}_{ij}}{\partial x_j}}\right| \tag{A.16}$$

$$\mu_t=\rho\nu_t \tag{A.17}$$

#### *A.1.3. Two-equation model: Standard $k-\varepsilon$*

The $k-\varepsilon$ model requires the use of a transport equation for turbulent kinetic energy ($k$ - Eq. (A.18)) and another transport equation for dissipation rate of kinetic energy ($\varepsilon$ - Eq. (A.19)). The constants in these equations are presented in Table A.2. The remaining necessary relationships for the k-epsilon model are presented in Eqs. (A.20) to (A.22).

$$\rho\frac{\partial k}{\partial t}+\rho\frac{\partial}{\partial x_i}\left(\bar{U}_i\,k\right)=\frac{\partial}{\partial x_i}\left(\left(\mu+\frac{\mu_t}{\sigma_k}\right)\frac{\partial k}{\partial x_i}\right)+P_k+P_{kb}-\rho\,\varepsilon \tag{A.18}$$

$$\rho\frac{\partial\varepsilon}{\partial t}+\rho\frac{\partial}{\partial x_i}\left(\bar{U}_i\,\varepsilon\right)=\frac{\partial}{\partial x_i}\left(\left(\mu+\frac{\mu_t}{\sigma_\varepsilon}\right)\frac{\partial\varepsilon}{\partial x_i}\right)+\frac{\varepsilon}{k}\left(C_{\varepsilon1}\left(P_k+P_{\varepsilon b}\right)-C_{\varepsilon2}\rho\,\varepsilon\right) \tag{A.19}$$

$$\mu_t=C_\mu\rho\frac{k^2}{\varepsilon} \tag{A.20}$$

$$P_k=\mu_t\left(\frac{\partial\bar{U}_i}{\partial x_j}+\frac{\partial\bar{U}_j}{\partial x_i}\right)\frac{\partial\bar{U}_i}{\partial x_j} \tag{A.21}$$

$$P_{kb}=-g_i\beta\frac{\mu_t}{\sigma_\theta}\frac{\partial\bar{T}}{\partial x_i} \tag{A.22}$$

$$P_{\varepsilon b}=g_i\frac{\mu_t}{\sigma_\theta}\frac{\partial\bar{T}}{\partial x_i} \tag{A.23}$$

#### *A.1.4. Two-equation model: $k-\omega$*

The $k-\omega$ model requires the use of a transport equation for turbulent kinetic energy ($k$ - Eq. (A.24)) and another transport equation for specific turbulence dissipation rate ($\omega$ - Eq. (A.25)). The constants used in these equations are presented in Table A.3. The remaining necessary relationships for the $k-\omega$ model are presented in Eqs. (A.26) and (A.27).

$$\rho\frac{\partial k}{\partial t}+\rho\frac{\partial}{\partial x_i}\left(\bar{U}_i,k\right)=\frac{\partial}{\partial x_i}\left(\left(\mu+\frac{\mu_t}{\sigma k}\right)\frac{\partial k}{\partial x_i}\right)+P_k+Pkb-\beta'\rho k,\omega \tag{A.24}$$

$$\begin{aligned}\rho\frac{\partial\omega}{\partial t}+\rho\frac{\partial}{\partial x_i}\left(\bar{U}_i,\omega\right)&=\frac{\partial}{\partial x_i}\left(\left(\mu+\frac{\mu_t}{\sigma_{\omega1}}\right)\frac{\partial\omega}{\partial x_i}\right)\\&+\frac{\omega}{k}\left(\left(\alpha'1P_k+P\omega b\right)-\beta'_1\rho k,\omega\right)\end{aligned} \tag{A.25}$$

$$\mu_t=\rho\frac{k}{\omega} \tag{A.26}$$

$$P_{\omega b}=P_{\varepsilon b}=g_i\frac{\mu_t}{\sigma_\theta}\frac{\partial\bar{T}}{\partial x_i} \tag{A.27}$$

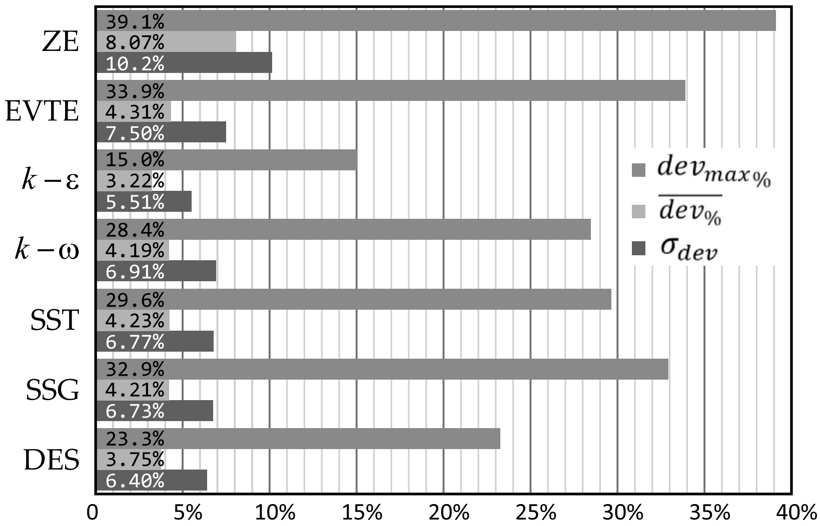

**Fig. 20.** Turbulence model comparison — highest deviation ($dev_{max_{\%}}$), mean deviation $\overline{dev_{\%}}$, and standard deviation ($\sigma_{dev}$) values for the ZE, EVTE, $k-\varepsilon$, $k-\omega$, SST, SSG and DES turbulence models.

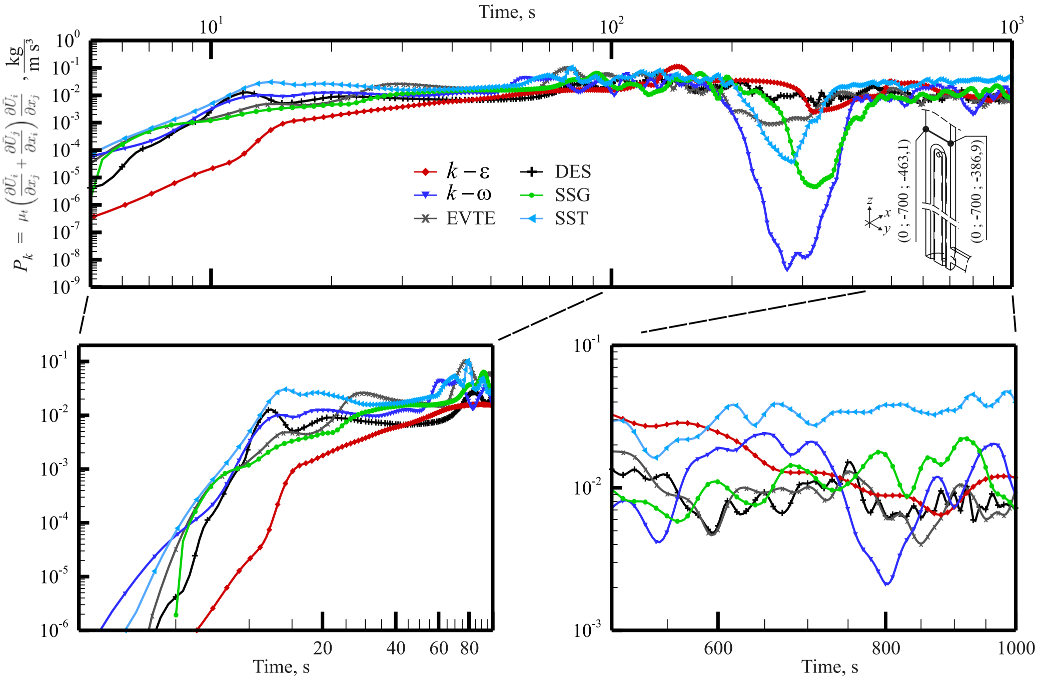

**Fig. 21.** Mean values (spatial average along the indicated line) of the turbulence production term as a function of time for the turbulence models: EVTE, $k-\varepsilon$, $k-\omega$, SST, SSG, and DES.

**Table A.1**
Eddy viscosity transport - constants.

| Constant | Value |
|---|---|
| $c_1$ | 0.144 |
| $c_2$ | 1.86 |
| $c_3$ | 7.0 |
| $A^+$ | 13.5 |
| $\kappa$ | 0.41 |
| $\hbar$ | 1.0 |

**Table A.2**
$k-\varepsilon$ model constants.

| Constant | Value |
|---|---|
| $C_\mu$ | 0.09 |
| $\sigma_k$ | 1.0 |
| $\sigma_\varepsilon$ | 1.3 |
| $\sigma_\theta$ | 0.9 |
| $C_{\varepsilon 1}$ | 1.44 |
| $C_{\varepsilon 2}$ | 1.92 |

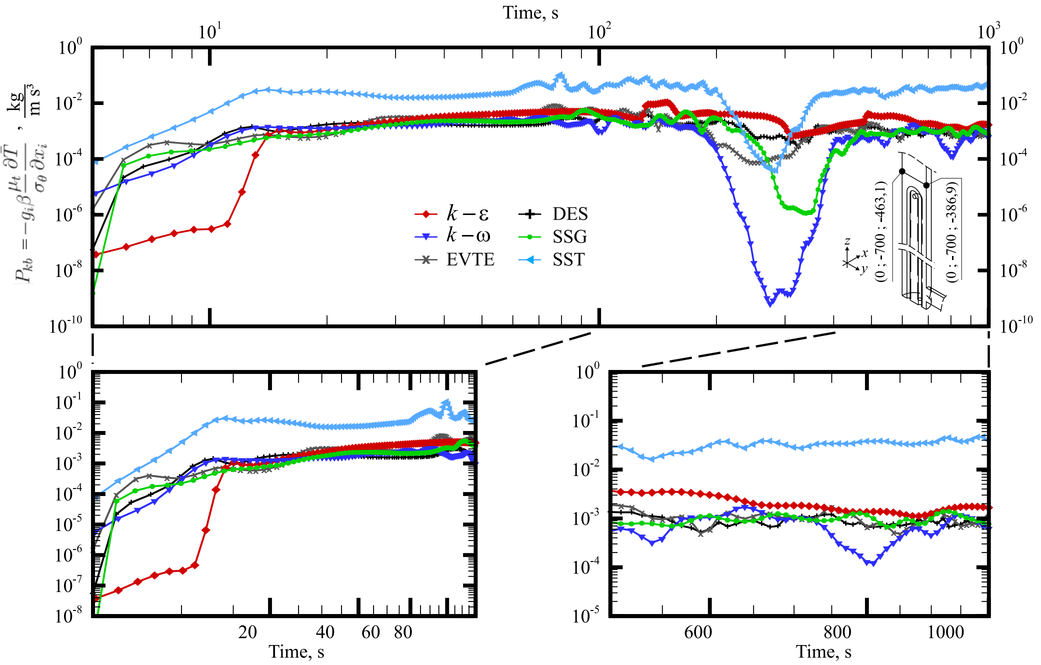

**Fig. 22.** Mean values (spatial average along the indicated line) of the buoyancy-related turbulent kinetic energy as a function of time for the turbulence models: EVTE, $k-\varepsilon$, $k-\omega$, SST, SSG, and DES.

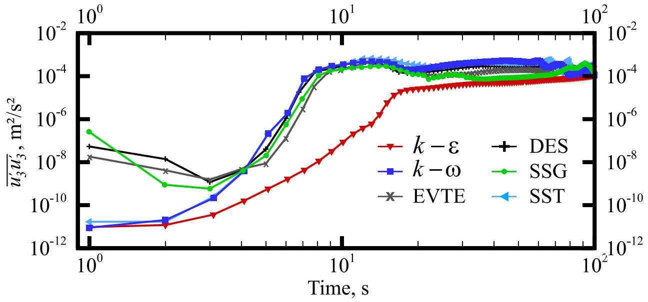

**Fig. 23.** Mean values (spatial average along the indicated line) for the temporal behavior of the product $\overline{u'_3u'_3}$ for the following turbulence models: EVTE, $k-\varepsilon$, $k-\omega$, SST, SSG, and DES.

### A.1.5. Two-equation model: Shear Stress Transport - SST

The SST model was proposed by Menter and Ames Research Center (1994), by coupling the $k-\omega$ and standard $k-\varepsilon$ formulations through blending functions. In the SST model, the transport equation for turbulent kinetic energy ($k$) remains as indicated in Eq. (A.24), and a new equation is proposed for $\omega$ as indicated in Eq. (A.28). The constants used in these equations are presented in Table A.4.

$$\rho\frac{\partial \omega}{\partial t} + \rho\frac{\partial}{\partial x_i}\left(\bar{U}_i\,\omega\right) = \frac{\partial}{\partial x_i}\left(\left(\mu + \frac{\mu_t}{\sigma_{\omega 3}}\right)\frac{\partial \omega}{\partial x_i}\right) + 2\rho(1-F_1)\,\frac{1}{\sigma_{\omega 2}\omega}\frac{\partial k}{\partial x_j}\frac{\partial \omega}{\partial x_j} + \frac{\omega}{k}\left(\left(\alpha'_3 P_k + P_{\omega b}\right) - \beta'_3\rho k\,\omega\right) \tag{A.28}$$

The coefficients for closing the transport equation and auxiliary relations are presented in Eqs. (A.29) to (A.33).

$$F_1 = \tanh\left\{\min\left[\max\left(\frac{\sqrt{k}}{\beta'\omega y}, \frac{500\,\nu}{y^2\omega}\right), \frac{4\rho k}{CD_{k\omega}\sigma_{\omega 2}y^2}\right]^4\right\} \tag{A.29}$$

where $y$ is the distance between the wall and the adjacent node.

$$F_2 = \tanh\left\{\left[\max\left(\frac{2\sqrt{k}}{\beta'\omega y}, \frac{500\,\nu}{y^2\omega}\right)\right]^2\right\} \tag{A.30}$$

$$CD_{k\omega} = \max\left(2\rho\frac{1}{\sigma_{\omega 2}\omega}\frac{\partial k}{\partial x_j}\frac{\partial \omega}{\partial x_j}, 1.0\times 10^{-10}\right) \tag{A.31}$$

$$P_k = \min\left(2\mu_t\bar{S}_{ij}\bar{S}_{ij}, 10\rho\,\beta' k\omega\right) \tag{A.32}$$

$$\mu_t = \frac{\rho\alpha' 1k}{\max\left(\alpha' 1\omega, F_2\sqrt{2\bar{S}ij\bar{S}ij}\right)} \tag{A.33}$$

The constants in the transport equations are obtained through linear combination, according to Eq. (A.34), using a generic constant $\phi$.

$$\phi_3 = F_1\phi_1 + \phi_2\left(1 - F_1\right) \tag{A.34}$$

### A.2. Reynolds stress-based model (SSG Reynolds stress)

In the SSG model, the Reynolds-averaged Navier–Stokes equation for the mean velocity remains as presented in Eq. (A.2), and the transport equation for the Reynolds stress tensors, as presented by Speziale et al. (1991) - Eq. (A.35). The constants used in the SSG model are presented in Table A.5, and the remaining necessary relationships for the SSG model are presented in Eqs. (A.36) to (A.41).

$$\rho\frac{\partial \overline{u'_iu'_j}}{\partial t} + \rho\frac{\partial}{\partial x_k}\left(\bar{U}_k\overline{u'_iu'_j}\right) + -\frac{\partial}{\partial x_k}\left(\left(\mu + \frac{2}{3}\rho C_S\frac{k^2}{\varepsilon}\right)\frac{\partial \overline{u'_iu'_j}}{\partial x_k}\right) = P_{ij} - \frac{2}{3}\delta_{ij}\rho\varepsilon + \Phi_{ij} + P_{ij,b} \tag{A.35}$$

$$P_{ij} = -\rho\overline{u'_lu'_k}\frac{\partial \bar{U}_j}{\partial x_k} - \rho\overline{u'_ju'_k}\frac{\partial \bar{U}_i}{\partial x_k} \tag{A.36}$$

$$P_{ij,b} = \frac{2}{3}\left(\frac{\mu_t}{\sigma_p}\beta g_k\frac{\partial T}{\partial x_k}\right)\delta_{ij} \tag{A.37}$$

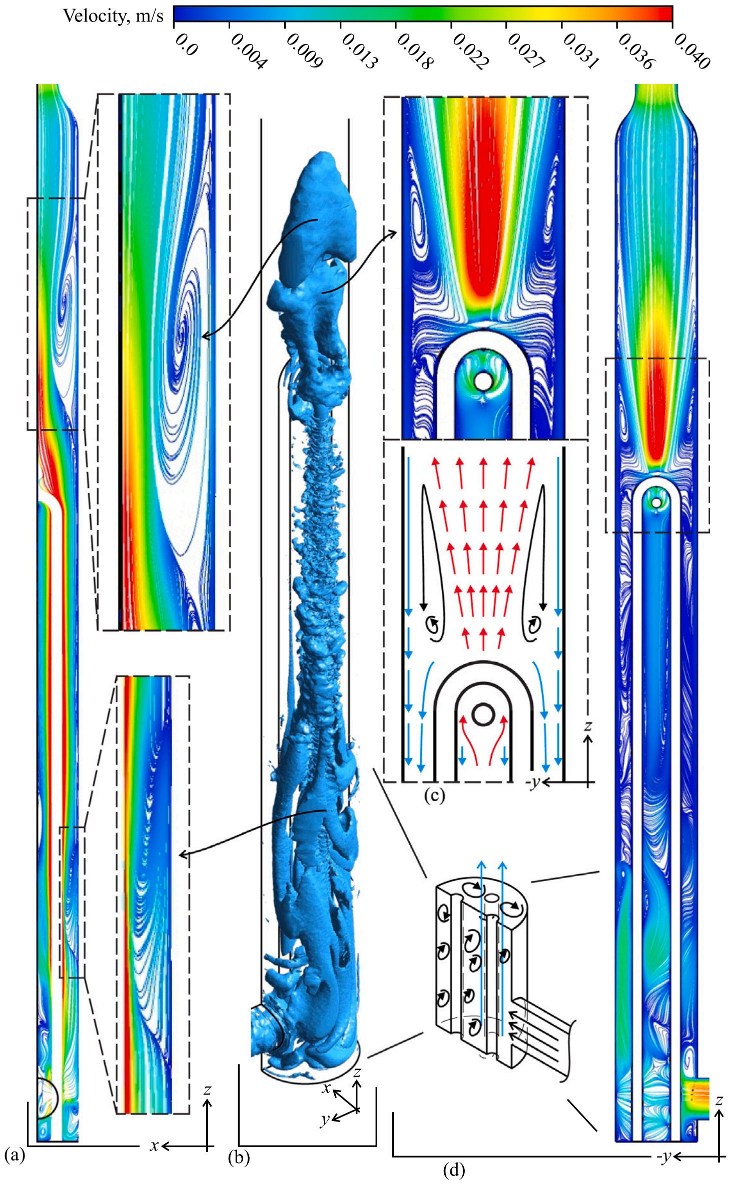

**Fig. 24.** Flow in the heater region — steady-state result for the DES model. The color maps demonstrate the intensity of the temporal mean velocity. (a) streamlines for the $xz$ plane, (b) Detail with invariant indication, (c) Schematic detail of the vortices in the upper portion of the heater, and (d) streamlines for the $yz$ plane.

$$\begin{aligned}\Phi_{ij} = & - \rho\varepsilon \left[ C_{S1} a_{ij} + C_{S2} \left( a_{ik} a_{kj} - \frac{1}{3} a_{mn} a_{mn} \delta_{ij} \right) \right] \\ & - C_{r1} a_{ij} \sqrt{2 P_{ij} P_{ij}} + C_{r2} \rho k \bar{S}_{ij} \\ & - C_{r3} \rho k \bar{S}_{ij} \sqrt{a_{mn} a_{mn}} + C_{r4} \rho k \left( a_{ik} \bar{S}_{jk} + a_{jk} \bar{S}_{ik} - \frac{2}{3} a_{kl} \bar{S}_{kl} \delta_{ij} \right) \\ & + C_{r5} \rho k \left( a_{ik} \bar{\Omega}_{jk} + a_{jk} \bar{\Omega}_{ik} \right)\end{aligned} \tag{A.38}$$

$$a_{ij} = \frac{\overline{u_i' u_j'}}{k} - \frac{2}{3} \delta_{ij} \tag{A.39}$$

$$\bar{\Omega}_{ij} = \frac{1}{2} \left( \frac{\partial \bar{U}_i}{\partial x_j} - \frac{\partial \bar{U}_j}{\partial x_i} \right) \tag{A.40}$$

$$\begin{aligned}& \rho \frac{\partial \varepsilon}{\partial t} + \rho \frac{\partial}{\partial x_k} \left( \bar{U}_k \varepsilon \right) = \\ & \frac{\varepsilon}{k} \left( c_{\varepsilon 1} \sqrt{2 P_{ij} P_{ij}} - c_{\varepsilon 2} \rho \varepsilon \right) + \frac{\partial}{\partial x_k} \left[ \left( \mu + \frac{\mu_t}{\sigma_{\varepsilon RS}} \right) \frac{\partial \varepsilon}{\partial x_k} \right]\end{aligned} \tag{A.41}$$

**Table A.3**
$k - \omega$ model constants.

| Constant | Value |
|---|---|
| $\beta'$ | 0.09 |
| $\alpha_1'$ | 5/9 |
| $\beta_1'$ | 0.075 |
| $\sigma_k$ | 2 |
| $\sigma_{\omega 1}$ | 2 |

### *A.3. Detached Eddy simulation model*

In this article, was used an formulation of Detached Eddy Simulation (DES) that combines the Large Eddy Simulation (LES) and Reynolds-averaged Navier–Stokes (RANS) SST model using cutoff functions between the models.

The theory proposed by LES consists of using spatial and temporal filters in the conservation equations. The filtered format of the governing equations is obtained, as presented in Eqs. (A.42), (A.43), and

**Table A.4**
SST model constants.

| | Constant$_1$ | Constant$_2$ |
|---|---|---|
| $\alpha'_{(i)}$ | 5/9 | 0.44 |
| $\beta'_{(i)}$ | 3/40 | 0.0828 |
| $\sigma_{\omega(i)}$ | 2 | 1/0.856 |

**Table A.5**
SSG model constants.

| Constant | Value |
|---|---|
| $\sigma_{\varepsilon RS}$ | 1.36 |
| $C_S$ | 0.22 |
| $c\varepsilon 1$ | 1.45 |
| $c_{\varepsilon 2}$ | 1.83 |
| $C_{S1}$ | 1.7 |
| $C_{S2}$ | −1.05 |
| $C_{r1}$ | 0.9 |
| $C_{r2}$ | 0.8 |
| $C_{r3}$ | 0.65 |
| $C_{r4}$ | 0.625 |
| $C_{r5}$ | 0.2 |
| $\sigma_p$ | 0.9 |

(A.44).

$$\frac{\partial \widetilde{U}_i}{\partial x_i} = 0 \tag{A.42}$$

$$\frac{\partial \widetilde{U}_i}{\partial t} + \frac{\partial}{\partial x_i}\left(\widetilde{U}_i \widetilde{U}_j\right) = -\frac{1}{\rho}\frac{\partial \widetilde{p}}{\partial x_i} + \nu \frac{\partial^2 \widetilde{U}_i}{\partial x_j \partial x_j} - \frac{\partial \widetilde{\tau}_{ij}}{\partial x_j} \tag{A.43}$$

$$\frac{\partial \widetilde{T}}{\partial t} + \frac{\partial}{\partial x_i}\left(\widetilde{U}_i \widetilde{T}\right) = \frac{\partial}{\partial x_i}\left(\alpha \frac{\partial \widetilde{T}}{\partial x_i} + \widetilde{U_i T} - \widetilde{U}_i \widetilde{T}\right) \tag{A.44}$$

Where $\widetilde{\tau_{ij}}$ is called the subgrid-scale stress tensor, defined by Eq. (A.45).

$$\widetilde{\tau_{ij}} = \widetilde{U_i U_j} - \widetilde{U}_i \widetilde{U}_j \tag{A.45}$$

$$-\widetilde{\tau}_{ij} - \frac{1}{3}\delta_{ij}\widetilde{\tau}_{kk} = 2\nu_{sgs}\left(\widetilde{S}_{ij}\right) = \nu_{sgs}\left(\frac{\partial \widetilde{U}_i}{\partial x_j} + \frac{\partial \widetilde{U}_j}{\partial x_i}\right) \tag{A.46}$$

$$-\alpha_{sgs}\frac{\partial \widetilde{T}}{\partial x_i} = \widetilde{U_i T} - \widetilde{U}_i \widetilde{T} \tag{A.47}$$

The DES model used in the simulations combines the two-equation SST model with the LES model in regions near walls and where large vortical structures are formed. Based on the turbulence length scale, the model switches between the two, as determined by Eqs. (A.48) and (A.49). Specifically, if the length scale exceeds the maximum element dimension ($\Delta$), the LES model is used; otherwise, SST is used. The SST model's turbulent kinetic energy equation is modified by replacing the destruction term with a function of the LES model's length scale, as shown in Eq. (A.50). The values of $L_t$, $\Delta$, and $F_{DES}$ are calculated using specific equations, and the constant $C_{DES}$ has a fixed value of 0.61.

$$L_t = \frac{k^{1/2}}{\beta' \omega} \tag{A.48}$$

$$\Delta = \max(\Delta x_1, \Delta x_2, \Delta x_3) \tag{A.49}$$

$$F_{DES} = \max\left(\frac{L_t}{C_{DES}\Delta}, 1\right) \tag{A.50}$$

## Appendix B. Nomenclature

| Symbol | Description |
|---|---|
| $Co$ | Courant number |
| $dev_{\%}$ | Deviation (%) |
| $\Delta l$ | Element volume edge length (m) |
| $\delta y$ | First cell height near the wall (m) |
| $f_\mu$ | Empirical damping function |
| $g$ | Gravitational acceleration (m/s$^2$) |
| $k$ | Turbulent kinetic energy (m$^2$/s$^2$) |
| $L$ | hydraulic diameter (m) |
| $L_{\upsilon K}$ | von Karman length (m) |
| $P_k$ | Turbulent kinetic energy production (Pa s$^{-1}$) |
| $P_{kb}$ | Buoyancy turbulent kinetic energy production (Pa s$^{-1}$) |
| $P_{\varepsilon b}$ | Buoyancy turbulent dissipation rate (m$^2$/s$^3$) |
| $p$ | Pressure (Pa) |
| $Ra$ | Rayleigh number |
| $S$ | Strain-rate tensor (1/s) |
| $S_M$ | Buoyancy source (N/m$^3$) |
| $t$ | Time (s) |
| $T$ | Temperature (K or °C) |
| $U$ | Velocity (m/s) |
| $\overline{u'_i T'}$ | Turbulent heat flux (K m/s) |
| $\overline{u'_i u'_j}$ | Reynolds stress tensor (m$^2$/s$^2$) |
| $y^+$ | Non-dimensional wall distance (m) |
| $\alpha$ | Thermal diffusivity (m$^2$/s) |
| $\beta$ | Volumetric thermal expansion coefficient (K$^{-1}$) |
| $\delta$ | Kronecker delta function |
| $\varepsilon$ | Turbulent dissipation rate (m$^2$/s$^3$) |
| $\mu$ | Dynamic viscosity (Pa s) |
| $\nu$ | Kinematic viscosity (m$^2$/s) |
| $\sigma_T$ | Total uncertainty |
| $\sigma_r$ | k-type uncertainty |
| $\sigma_m$ | Standard deviation |
| $\rho$ | Density (kg/m$^3$) |
| Subscripts | |
| $exp$ | Experimental measurement |
| $i, j, k$ | Index for direction |
| $ref$ | Reference |
| $t$ | Turbulent quantity |
| $max$ | Maximum value |
| $min$ | Minimum value |
| $N$ | Numerical value |
| $sgs$ | Subgrid-scale quantity |
| Overscripts | |
| $\Phi'$ | Fluctuating component |
| $\overline{\Phi}$ | Time-averaged |
| $\widetilde{\Phi}$ | Filtered quantity |

## References

Adinarayana, K., Mangarjuna Rao, P., Ali, S.M., 2022. Numerical investigations on dynamic characteristics of series coupled single-phase natural circulation loops. Int. J. Therm. Sci. 181, 107717. http://dx.doi.org/10.1016/j.ijthermalsci.2022.107717.

Angelo, G., Andrade, D., Angelo, E., Torres, W., Sabundjian, G., Macedo, L., Silva, A., 2012. A numerical and three-dimensional analysis of steady state rectangular natural circulation loop. Nucl. Eng. Des. 244, 61–72. http://dx.doi.org/10.1016/j.nucengdes.2011.12.020.

Basu, D.N., Bhattacharyya, S., Das, P., 2012. Performance comparison of rectangular and toroidal natural circulation loops under steady and transient conditions. Int. J. Therm. Sci. 57, 142–151. http://dx.doi.org/10.1016/j.ijthermalsci.2012.02.011.

Bueno, R., Masotti, P., Justo, J., Andrade, D., Rocha, M., Torres, W., de Mesquita, R., 2018. Two-phase flow bubble detection method applied to natural circulation system using fuzzy image processing. Nucl. Eng. Des. 335, 255–264. http://dx.doi.org/10.1016/j.nucengdes.2018.05.026.

Carelli, M.D., Conway, L., Oriani, L., Petrović, B., Lombardi, C., Ricotti, M., Barroso, A., Collado, J., Cinotti, L., Todreas, N., Grgić, D., Moraes, M., Boroughs, R., Ninokata, H., Ingersoll, D., Oriolo, F., 2004. The design and safety features of the IRIS reactor. Nucl. Eng. Des. 230 (1), 151–167. http://dx.doi.org/10.1016/j.nucengdes.2003.11.022, 11th International Conference on Nuclear Energy.

CFX-Solver ANSYS, 2006. Theory guide. Release ll.

Cheng, H., Lei, H., Dai, C., 2018. Thermo-hydraulic characteristics and second-law analysis of a single-phase natural circulation loop with end heat exchangers. Int. J. Therm. Sci. 129, 375–384. http://dx.doi.org/10.1016/j.ijthermalsci.2018.03.026.

Conti, T.d.N., Sabundjian, G., Torres, W.M., Macedo, L.A., Andrade, D.A., Umbehaun, P.E., Mesquita, R.N., 2011. Study of the natural circulation phenomenon for nuclear reactors. In: AIP Conference Proceedings, Vol. 1351, No. 1. American Institute of Physics, pp. 391–396. http://dx.doi.org/10.1063/1.3608994.

Darwish, M., Moukalled, F., 2016. The Finite Volume Method in Computational Fluid Dynamics: An Advanced Introduction with OpenFOAM® and Matlab®. Springer.

de Mesquita, R.N., Castro, L.F., Torres, W.M., da S. Rocha, M., Umbehaun, P.E., Andrade, D.A., Sabundjian, G., Masotti, P.H., 2018. Classification of natural circulation two-phase flow image patterns based on self-organizing maps of full frame DCT coefficients. Nucl. Eng. Des. 335, 161–171. http://dx.doi.org/10.1016/j.nucengdes.2018.05.019.

de Mesquita, R., Masotti, P., Penha, R., Andrade, D., Sabundjian, G., Torres, W., Macedo, L., 2012. Classification of natural circulation two-phase flow patterns using fuzzy inference on image analysis. Nucl. Eng. Des. 250, 592–599. http://dx.doi.org/10.1016/j.nucengdes.2012.06.014.

Devia, F., Misale, M., 2012. Analysis of the effects of heat sink temperature on single-phase natural circulation loops behaviour. Int. J. Therm. Sci. 59, 195–202. http://dx.doi.org/10.1016/j.ijthermalsci.2012.03.006.

Elton, D., Arunachala, U., Vijayan, P., 2022. Stability performance of series coupled natural circulation system with different operating procedures. Int. J. Therm. Sci. 179, 107693. http://dx.doi.org/10.1016/j.ijthermalsci.2022.107693.

Greif, R., 1988. Natural circulation loops. J. Heat Transfer 110 (4b), 1243–1258. http://dx.doi.org/10.1115/1.3250624.

Huang, B.J., Zelaya, R., 1988. Heat transfer behavior of a rectangular thermosyphon loop. J. Heat Transfer 110 (2), 487–493. http://dx.doi.org/10.1115/1.3250512.

Incropera, F., DeWitt, D., 1985. Introduction to Heat Transfer. John Wiley and Sons Inc., New York, NY.

Ji, R., Wenig, P.J., Kelm, S., Klein, M., 2023. Epistemic uncertainty in URANS based CFD analysis of buoyancy driven flows—Comparison of URANS and LES. Ann. Nucl. Energy 181, 109563. http://dx.doi.org/10.1016/j.anucene.2022.109563.

Jiang, Y.Y., Shoji, M., Naruse, M., 2002. Boundary condition effects on the flow stability in a toroidal thermosyphon. Int. J. Heat Fluid Flow 23 (1), 81–91. http://dx.doi.org/10.1016/S0142-727X(01)00141-2.

Kelly, J.E., 2014. Generation IV international forum: A decade of progress through international cooperation. Prog. Nucl. Energy 77, 240–246. http://dx.doi.org/10.1016/j.pnucene.2014.02.010.

Kelm, S., Lehmkuhl, J., Jahn, W., Allelein, H.-J., 2016. A comparative assessment of different experiments on buoyancy driven mixing processes by means of CFD. Ann. Nucl. Energy 93, 50–57. http://dx.doi.org/10.1016/j.anucene.2015.12.032, ERMSAR-2015 conference of SARNET in the frame of the NUGENIA Technical Area 2. URL https://www.sciencedirect.com/science/article/pii/S0306454915300426.

Kim, S.Y., Shin, D.H., Kim, C.S., Park, G.C., Cho, H.K., 2021. Computational fluid dynamics analysis of buoyancy-aided turbulent mixed convection inside a heated vertical rectangular duct. Prog. Nucl. Energy 137, 103766. http://dx.doi.org/10.1016/j.pnucene.2021.103766.

Kolář, V., 2011. Detection problems of vortical structures. In: HEFAT 2011. International Conference on Heat Transfer, Fluid Mechanics and Thermodynamics.

Krishnani, M., Basu, D.N., 2016. On the validity of Boussinesq approximation in transient simulation of single-phase natural circulation loops. Int. J. Therm. Sci. 105, 224–232. http://dx.doi.org/10.1016/j.ijthermalsci.2016.03.004.

Kudariyawar, J.Y., Srivastava, A.K., Vaidya, A.M., Maheshwari, N.K., Satyamurthy, P., 2016a. Computational and experimental investigation of steady state and transient characteristics of molten salt natural circulation loop. Appl. Therm. Eng. 99, 560–571. http://dx.doi.org/10.1016/j.applthermaleng.2015.12.114.

Kudariyawar, J.Y., Vaidya, A.M., Maheshwari, N.K., Satyamurthy, P., 2016b. Computational study of instabilities in a rectangular natural circulation loop using 3D CFD simulation. Int. J. Therm. Sci. 101, 193–206. http://dx.doi.org/10.1016/j.ijthermalsci.2015.11.003.

Launder, B., Sharma, B., 1974. Application of the energy-dissipation model of turbulence to the calculation of flow near a spinning disc. Lett. Heat Mass Transfer 1 (2), 131–137. http://dx.doi.org/10.1016/0094-4548(74)90150-7.

Menter, F.R., 1994. Two-equation eddy-viscosity turbulence models for engineering applications. AIAA J. 32 (8), 1598–1605. http://dx.doi.org/10.2514/3.12149.

Menter, F.R., 1997. Eddy viscosity transport equations and their relation to the k-$\varepsilon$ model. J. Fluids Eng. 119 (4), 876–884. http://dx.doi.org/10.1115/1.2819511.

Menter, F.R., Ames Research Center, 1994. Eddy Viscosity Transport Equations and Their Relation to the k-$\varepsilon$. National Aeronautics and Space Administration, Ames Research Center, p. 1 v., URL https://nla.gov.au/nla.cat-vn4105715.

Pilkhwal, D., Ambrosini, W., Forgione, N., Vijayan, P., Saha, D., Ferreri, J., 2007. Analysis of the unstable behaviour of a single-phase natural circulation loop with one-dimensional and computational fluid-dynamic models. Ann. Nucl. Energy 34 (5), 339–355. http://dx.doi.org/10.1016/j.anucene.2007.01.012.

Piña-Ortiz, A., Hinojosa, J., Maytorena, V., 2014. Test of turbulence models for natural convection in an open cubic tilted cavity. Int. Commun. Heat Mass Transfer 57, 264–273. http://dx.doi.org/10.1016/j.icheatmasstransfer.2014.08.011.

Rogers, G., Mayhew, Y., 1964. Heat transfer and pressure loss in helically coiled tubes with turbulent flow. Int. J. Heat Mass Transfer 7 (11), 1207–1216. http://dx.doi.org/10.1016/0017-9310(64)90062-6.

Ryu, K.H., Ban, B.M., Lee, T.H., Lee, J., Lee, S.H., Cho, J.H., ho Ko, S., Kim, J.H., 2018. Natural circulation characteristics under various conditions on heavy liquid metal test loop. Int. J. Therm. Sci. 132, 316–321. http://dx.doi.org/10.1016/j.ijthermalsci.2018.06.015.

Sabundjian, G., Andrade, D.A.d., Umbehaun, P.E., Torres, W.M., Macedo, L.A., Conti, T.N., Mesquita, R.N.d., Angelo, G., 2011. Comparison between experimental data and numerical modeling for the natural circulation phenomenon. J. Braz. Soc. Mech. Sci. Eng. 33, 227–232. http://dx.doi.org/10.1590/S1678-58782011000500003.

Sagaut, P., 2006. Large Eddy Simulation for Incompressible Flows: An Introduction. Springer Science & Business Media.

Sahu, M., Sarkar, J., Chandra, L., 2023. Experimental thermal-hydraulic characteristics of single-phase natural circulation loop using water-based hybrid nanofluids. Int. J. Therm. Sci. 187, 108198. http://dx.doi.org/10.1016/j.ijthermalsci.2023.108198.

Sarkar, M.K., Basu, D.N., 2017. Numerical appraisal on the suitability of supercritical condition in natural circulation loop with isothermal boundary conditions. Int. J. Therm. Sci. 111, 30–40. http://dx.doi.org/10.1016/j.ijthermalsci.2016.08.002.

Speziale, C.G., Sarkar, S., Gatski, T.B., 1991. Modelling the pressure–strain correlation of turbulence: an invariant dynamical systems approach. J. Fluid Mech. 227, 245–272. http://dx.doi.org/10.1017/S0022112091000101.

Spiga, M., Vocale, P., 2015. Step response for free convection between parallel walls. Heat Mass Transf. 51, 1761–1768. http://dx.doi.org/10.1007/s00231-015-1539-x.

Stern, F., Wilson, R.V., Coleman, H.W., Paterson, E.G., 2001. Comprehensive approach to verification and validation of CFD simulations—Part 1: Methodology and procedures. J. Fluids Eng. 123 (4), 793–802. http://dx.doi.org/10.1115/1.1412235.

Talaat, K., Chen, M., 2023. Design of a prototypical natural circulation water-based reactor cavity cooling system (RCCS) for a pebble-bed generic FHR. Nucl. Eng. Des. 407, 112303. http://dx.doi.org/10.1016/j.nucengdes.2023.112303.

Vijayan, P., 2002. Experimental observations on the general trends of the steady state and stability behaviour of single-phase natural circulation loops. Nucl. Eng. Des. 215 (1), 139–152. http://dx.doi.org/10.1016/S0029-5493(02)00047-X.

Walsh, P., Leong, W., 2004. Effectiveness of several turbulence models in natural convection. Internat. J. Numer. Methods Heat Fluid Flow 14 (5), 633–648. http://dx.doi.org/10.1108/09615530410539955.

Wilcox, D.C., et al., 1998. Turbulence Modeling For CFD, vol. 2, DCW industries La Canada, CA.

Wilson, R.V., Stern, F., Coleman, H.W., Paterson, E.G., 2001. Comprehensive approach to verification and validation of CFD simulations—Part 2: Application for rans simulation of a cargo/container ship. J. Fluids Eng. 123 (4), 803–810. http://dx.doi.org/10.1115/1.1412236.

Zvirin, Y., 1982. A review of natural circulation loops in pressurized water reactors and other systems. Nucl. Eng. Des. 67 (2), 203–225. http://dx.doi.org/10.1016/0029-5493(82)90142-X.